IEEE Access
Multidisciplinary ⋮ Rapid Review ⋮ Open Access Journal

Received 17 August 2023, accepted 18 September 2023, date of publication 25 September 2023, date of current version 3 October 2023.

Digital Object Identifier 10.1109/ACCESS.2023.3318527

RESEARCH ARTICLE

A Comprehensive Analytical Sizing Methodology for Transverse and Radial Flux Machines

VÍCTOR BALLESTÍN-BERNAD[1], ARITZ EGEA-CÁCERES[2], JESÚS SERGIO ARTAL-SEVIL[1], AND JOSÉ ANTONIO DOMÍNGUEZ-NAVARRO[1], (Senior Member, IEEE)

[1]Department of Electrical Engineering, University of Zaragoza, 50018 Zaragoza, Spain
[2]Department of Electronics and Computer Science, Mondragon University, 20500 Arrasate/Mondragón, Spain

Corresponding author: José Antonio Domínguez-Navarro (jadona@unizar.es)

This work was supported in part by the Spanish Ministry of Universities under Grant FPU20/03436.

ABSTRACT Transverse flux machines have the potential to offer high torque density in direct-drive vehicle traction applications. Besides, sizing equations are a wide-spread technique for transverse flux machines design, as their computational cost is much lower than the finite element method. In this paper a novel analytical sizing methodology for transverse and radial flux machines is presented, focusing on the current load and the pole length factor as the main design parameters. The motor specifications are intended for a light-duty electric vehicle application. As transverse flux machines have a single, hoop-shaped coil per phase that embraces the flux of all the pole pairs, their principle of operation and therefore their sizing equations differ from radial flux machines. The proposed analytical method allows to compare transverse and radial flux machines easily through a similarity analysis and a parametric study. Furthermore, the discrepancies between the analytical model and the finite element method are quantified and then included in previous equations. Then the analytical model is optimized with a multiobjective genetic algorithm in the final stage. According to the sizing methodology presented here, transverse flux machines have a superior performance than radial flux machines in terms of torque density and efficiency.

INDEX TERMS Analytical sizing equations, electric vehicles, finite element method, multiobjective genetic algorithm, permanent magnet synchronous machines, transverse flux machines.

NOMENCLATURE

A_s	Stator current load, RMS.
a_s	Number of parallel paths in the stator.
$\hat{B}_0$	No-load flux density, peak value.
$\overline{B}_0$	No-load flux density, mean value.
$\hat{B}_{01}$	No-load flux density, peak value of the first harmonic.
$\hat{B}_{aq}$	q-axis armature flux density, peak value.
$\overline{B}_{aq}$	q-axis armature flux density, mean value.
$\hat{B}_{aq1}$	q-axis armature flux density, peak value of the first harmonic.
$\hat{B}_m$	Magnets remanence, peak value.
B_{ry}	Flux density in the rotor yoke.
B_{sb}	Flux density in the stator bridges.
B_{sta}	Apparent flux density in the stator tooth.
B_{sy}	Flux density in the stator yoke.
D_g	Gap diameter.
D_i	Inner diameter.
D_o	Outer diameter.
d_{Fe}	Iron density.
d_m	Magnets density.
d_{Cu}	Copper density.
e_0	Back-EMF, per unit.
E_0	Back-EMF, RMS.
g_a	Air gap length.
g_d	d-axis gap.
g_m	Magnets radial length.
g_q	q-axis gap.
h_{ry}	Rotor yoke height.

The associate editor coordinating the review of this manuscript and approving it for publication was Xiaodong Liang.

h_{sb}	Stator bridge height.
h_{ss}	Stator slot height.
h_{sso}	Stator slot opening height.
h_{ssw}	Stator slot wedge height.
h_{sy}	Stator yoke height.
$\hat{I}_d$	Stator current in the d-axis, peak value.
$\hat{I}_q$	Stator current in the q-axis, peak value.
I_s	Stator current, RMS.
J_s	Stator current density, RMS.
k_0	FEM no-load factor.
k_{0f}	FEM no-load form factor.
k_{0pk}	FEM no-load peak factor.
$k_{0\Psi}$	FEM no-load flux factor.
k_a	FEM armature factor.
k_{af}	FEM armature form factor.
k_{apk}	FEM armature peak factor.
$k_{a\Psi}$	FEM armature flux factor.
k_C	Carter factor.
k_{Cu}	Copper fill factor.
k_{fr1}	Form factor of the rotor, 1st harmonic.
k_{fs1}	Form factor of the stator, 1st harmonic.
k_{gma}	Magnets-to air gap ratio.
k_l	Pole length factor.
k_{loDo}	Outer-length-to-outer-diameter ratio.
k_N	Equivalent turns factor.
k_r	Rotor factor.
k_s	Stator factor.
k_{sat}	Saturation factor.
k_{Sp}	Pole surface factor.
k_{ss}	Stator slot aspect ratio.
k_{wss}	Stator slot width factor.
k_σ	Leakage factor.
L_d	d-axis inductance.
L_q	q-axis inductance.
L_{qm}	q-axis magnetizing inductance.
L_σ	Leakage inductance.
l	Pole length.
l_m	Phase length.
l_{Ns}	Turn length.
l_o	Outer length.
m	Number of phases.
m_a	Active mass.
N_{ms}	Stator number of turns per phase.
N_{Qs}	Stator number of turns per slot.
n_1	Base speed.
P	Peak motor power.
P_{Cu}	Copper losses.
P_{Fe1}	Iron losses, first harmonic.
p	Number of pole pairs.
q_s	Number of stator slots per pole and phase.
Q_s	Number of stator slots.
R_{ms}	Stator resistance per phase.
R_{th}	Thermal resistance.
S_{ss}	Stator slot cross-section.
T_1	Peak motor torque at the base speed.
U_{DC}	DC-voltage.
U_s	Stator voltage, RMS.
V_m	Magnets volume.
V_o	Outer volume.
V_r	Rotor volume.
V_{ry}	Rotor yoke volume.
V_{sb}	Stator bridges volume.
V_{st}	Stator teeth volume.
V_{sy}	Stator yoke volume.
V_{Cu}	Copper volume.
w_{ss}	Stator slot width.
w_{sso}	Stator slot opening width.
w_{st}	Stator tooth width.
w_{st1}	Stator tooth width in the stator bridge (TFM).
w_{st2}	Stator tooth width in the stator yoke (TFM).
α_r	Rotor span angle.
α_s	Stator span angle.
α_{sso}	Stator slot opening angle.
α_{th}	Thermal transfer coefficient.
ΔT	Temperature rise.
δ_i	Current phasor angle with respect to the q-axis.
η	Efficiency.
λ_{ew}	Specific permeance of the end-winding.
λ_{sb}	Specific permeance of the stator bridge.
λ_{ss}	Specific permeance of the stator slot.
λ_{sso}	Specific permeance of the stator slot opening.
λ_{ssw}	Specific permeance of the stator slot wedge.
λ_{tt}	Specific permeance of the tooth tip.
μ_0	Vacuum permeabiliy.
μ_{rm}	Relative permeabiliy of the magnets.
ω_1	Base angular frequency.
φ	Power factor angle.
$\hat{\Phi}_0$	No-load flux, peak value.
$\hat{\Psi}_0$	No-load flux linkage, peak value.
$\hat{\Psi}_{aq}$	Magnetizing armature q-axis flux linkage, peak value.
ρ_{Cu}	Copper resistivity.
τ_p	Pole pitch.
τ_{Qs}	Stator slot pitch.
ξ_{r1}	Winding factor of the rotor, 1st harmonic.
ξ_{s1}	Winding factor of the stator, 1st harmonic.
EMF	Electromotive force.
FEM	Finite element method.
PM	Permanent magnet.
PMSM	Permanent magnet synchronous machine.
RFM	Radial flux machine.
S-PMSM	Permanent magnet synchronous machine with flux-concentrating PMs.
TFM-U	Transverse flux machine with U-cores.
TFM	Transverse flux machine.
$^{(R)}$	Radial flux machine.
$^{(T)}$	Transverse flux machine.
*	Similarity between transverse and radial flux machines.

I. INTRODUCTION

Transverse flux machines (TFMs) have the potential to offer high torque density in direct-drive applications such as electric vehicles, wind power and fault-tolerant aircraft

generators [1]. TFMs benefit from magnetic and electrical loadings being decoupled, resulting in high torque density [2]. However, their design and operation are still challenging regarding torque ripple and power factor [3], [4]. Moreover, TFMs have been seen traditionally as difficult to manufacture due to their complex structure, but in the last few years additive manufacturing is opening up new posssibilies regarding the housing design, in order to accommodate a large number of pieces and facilitate cooling, and improvements in electromagnetic performance with the use of soft magnetic materials [5], [6].

As TFMs design methods based on the finite element method (FEM) require 3D, time-consuming models, sizing equations or magnetic equivalent circuits are generally used for preliminary analysis, at the cost of offering lower accuracy than FEM. In [2] the authors present some sizing equations based on the gap-to-outer diameter ratio, with a remarkable effort to integrate different voltage, current and power waveforms in sizing equations. The analysis is limited to the optimal power density output for different speeds using both rare-earth and ferrite magnets, with the rare-earth TFM showing a better performance than the induction machine in terns of power density. This method has been expanded to other TFMs in [7], [8], and [9]. The sizing equations presented in [10] and [11] are more accurate, but not straightforward, being based on the complex permeance method to obtain the flux density distribution in the air gap, then the torque is calculated introducing a flux factor that takes into account the effective air gap flux that produces torque. Furthermore, TFMs sizing is addressed using a magnetic equivalent circuit (MEC) in [12], [13], [14], [15], and [16] TFMs modeling is based on a position-dependent air gap flux density and MEC. A TFM with a single-row of magnets is proposed in [13]: validation of MEC with no-load tests shows a 9 % discrepancy in the back-EMF, while FEM shows a great agreement with tests. However, FEM versus experimental error becomes higher under load, and the same conclusion is drawn in [17]. The authors of [18] propose a two-phase TFM with skewed PMs and shared-border pole stator, showing a 2.6 % error between FEM and experimental effective values of the back-EMF. Besides, magnetic charge method has been also proved as feasible for TFMs design [19] even though it has not been widely used in the literature.

TFMs have been explored for electric vehicle applications such as e-scooters [20], [21], [22], hybrid cars [23], hybrid buses [24] and ships [25]. Recently a claw-pole TFM has been integrated in a commercial motorcycle [26], [27]. TFMs efficiency has been proved similar to RFMs in the low-speed, low-torque range, being superior for TFMs in high-torque points and lower in high-speed points [28]. However, the overload capability, power factor and efficiency of TFMs must still be improved to compete with radial flux machines performance [29]. In [30] three transverse, radial and axial flux machines with the same dimensions and permanent magnet (PM) mass are compared, with the TFM showing a greater torque for low current load, but poor flux-weakening capabilities.

In this work a comprehensive analytical sizing methodology for transverse and radial flux machines is presented. The motor specifications are based on a light-duty electric vehicle, without loss of generality. The model is based on a first-harmonic analysis as a trade-off between accuracy and complexity, and then the underlying assumptions are verified via FEM. All the main dimensions and parameters have been considered in the analysis, not just the outer dimensions as usually done in the literature. Furthermore, the equations are easily adaptable to different transverse and radial flux machine topologies, thus allowing a more straightforward and general analysis than previous gap-to-outer diameter analytical models or magnetic equivalent circuits. The proposed equations have a similar form for transverse and radial flux machines, thus allowing to deduce the similarity equations presented here in order to compare both topologies. It means that, given some specifications and design parameters, most of the TFM dimensions can be calculated from a base radial machine applying the similarity equations.

This document is structured as follows. In Section II the main dimensions and sizing equations of TFMs and RFMs are deduced for each of the stator and rotor components. Section III deals with the similarity equations, stating that the TFM has an extra degree of freedom for design, and the parametric study, with the pole length ratio and current load as the main design parameters. In Section IV the discrepancies between the analytical method and FEM are quantified by defining different FEM factors. In Section V the analytical model is optimized, including surface-fitted FEM factors, and Section VI concludes the paper with a brief summary.

II. SIZING EQUATIONS FOR TRANSVERSE AND RADIAL FLUX MACHINES

Conventional radial flux machines (RFMs) and axial flux machines (AFMs) start from a similar concept, as the flux of each pole goes through the coils, distributed in slots, and then the flux linkage of all the series-connected coils in a phase is added up. However, in TFMs there is a unique, concentrated coil per phase that links the flux of all the poles at the same time. In all cases, if the gap diameter is kept constant and the pole pairs are duplicated, the pole section is halved (1). As RFMs and AFMs are generally formed by the series connection of the coils, the number of turns per phase has to be duplicated in order to keep constant the no-load flux linkage (2) and so the back-EMF and torque. However, in TFMs the hoop-shaped coil embraces the flux of all the pole pairs in a phase, so the halving of the pole section is compensated by the duplication of the pole pairs, then an increase in the number of turns results in a multiplication of the back-EMF and torque. Therefore, TFMs take advantage of a high number of pole pairs to deliver high torque. Besides, hybrid machines that combine some features from TFMs and RFMs have been proved recently as a good alternative

in order to increase further torque and torque density with respect to conventional induction machines and permanent magnet synchronous machines [31], [32].

$$S_p = \tau_p l = \frac{\pi D_g}{2p} l \tag{1}$$

$$\hat{\Psi}_0 \propto \begin{cases} N_{ms} S_p p & \text{for TFMs} \\ N_{ms} S_p & \text{for RFMs} \end{cases} \tag{2}$$

The main parts of the magnetic circuit of TFMs and RFMs and their dimensions are shown in Figure 1. In TFMs the flux path is essentially perpendicular (i.e. "transverse") to the rotation plane, so the magnetic and electrical loadings are decoupled. Thereby the stator span α_s is chosen in a similar way as the rotor span, according to (3), in order to prevent leakage flux. Both rotors in Figure 1 correspond to a surface permanent magnet synchronous motor (S-PMSM), in which the equivalent d-axis gap is the sum of the magnets radial height g_m and the air gap g_a corrected with the PMs relative permeability μ_{rm} and the Carter factor k_C, respectively. As the PMs permeability is close to that of air, both the d- and q-axis equivalent gaps are assumed to be equal. Here the magnets-to-air gap ratio (5) has been introduced, as it is practical for sizing purposes: in Section II-B it will be shown that the no-load flux density in the air gap depends only on the PMs remanence and the magnets-to-air gap ratio.

$$k_r = \frac{\alpha_r D_g/2}{\tau_p} \tag{3}$$

$$g_d = g_m/\mu_{rm} + k_C g_a = k_C g_a \left(1 + k_{gma}\right) \simeq g_q \tag{4}$$

$$k_{gma} = \frac{g_m/\mu_{rm}}{k_C g_a} \tag{5}$$

A. SPECIFICATIONS

Table 1 shows the main specifications of the electrical motors that have been designed in this paper. This values correspond to a light-duty electric vehicle application, according to literature. As the aim is to compare TFMs and RFMs for direct-drive vehicle traction applications, unit transmission ratio has been considered. Figure 2 shows the phasor diagram of a S-PMSM in its maximum torque operating point, that is, according to (6), when the stator peak current is fully aligned with the q-axis. At other operating points, the stator current phasor forms an angle δ_i with the q-axis (7). The electrical angular frequency is given by (8) as a function of the rated speed and the number of pole pairs. The RMS value of the stator voltage is related to the DC-bus voltage, as in electric vehicles the motor is fed by a power converter: in this work the peak voltage of the extended sine-triangle or space vector modulation techniques at their maximum modulation index has been considered for calculations (9) [33]. Once the stator RMS voltage is known, the back-EMF and the power factor angle can be calculated (10) and finally the no-load flux linkage (11) and the inductances (12), (13).

$$T_1 = \frac{m}{2} p \hat{\Psi}_0 \hat{I}_q \tag{6}$$

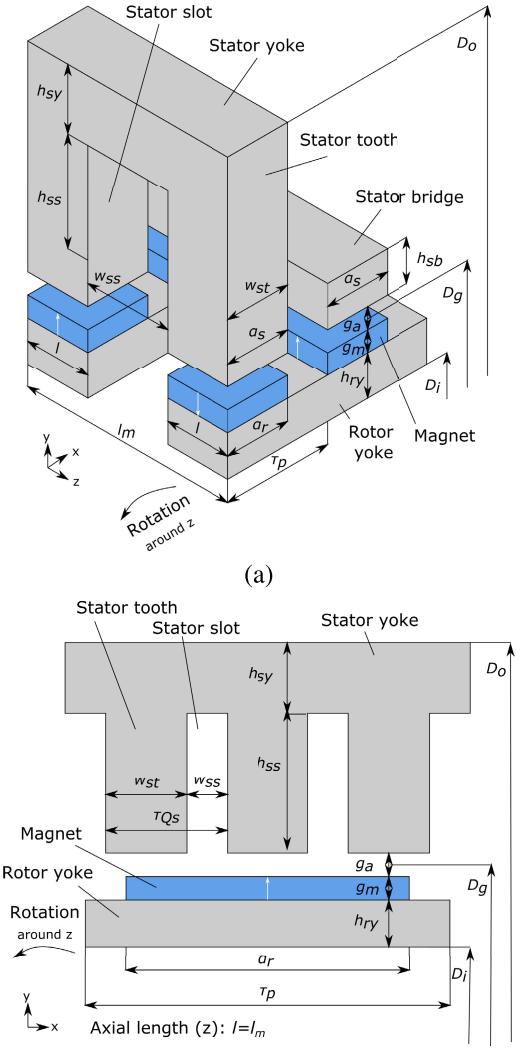

FIGURE 1. Linear view and main dimensions of: (a) TFMs, (b) RFMs with $q_s = 1$.

$$\hat{I}_d = -\sqrt{2} I_s \sin \delta_i$$

$$\hat{I}_q = \sqrt{2} I_s \cos \delta_i \tag{7}$$

$$\omega_1 = p \frac{2\pi}{60} n_1 \tag{8}$$

$$\sqrt{2} U_s = \frac{U_{DC}}{\sqrt{3}} \tag{9}$$

$$\varphi = \arccos \frac{E_0}{U_s} = \arccos e_0 \tag{10}$$

$$\sqrt{2} E_0 = \xi_{s1} \hat{\Psi}_0 \omega_1 \tag{11}$$

$$\tan \varphi = \frac{L_q \omega_1 I_s}{E_0} \tag{12}$$

$$L_q = L_d \tag{13}$$

In conventional RFMs both the stator and rotor cores are made of electrical steel laminations, whereas in TFMs the use of soft magnetic composites is progressively gaining wider attention [34], [35]. Table 2 shows some representative values

TABLE 1. Specifications of TFMs and RFMs.

	TFM	RFM
Peak power, P	4 kW	
Number of phases, m	3	
Motor:wheel speed ratio	1:1	
Base speed, n_1	500 rpm	
Maximum vehicle speed	80 km/h	
Pole pairs, p	10	2
DC-voltage, U_{DC}	48 V	
Back-EMF, e_0	0.8 p.u.	
Peak current (RMS), I_s	85 A	
Rotor arrangement	Surface magnets	
No-load flux linkage, $\hat{\Psi}_0$	42.3 mWb	212 mWb
Inductance, $L_d = L_q$	0.27 mH	1.4 mH

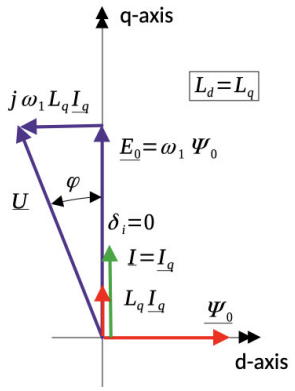

FIGURE 2. Phasor diagram of a S-PMSM for maximum torque.

TABLE 2. Design parameters related to material properties.

Magnets (N30H)	Remanent flux density, $\hat{B}_m$	1.12
	Relative permeability, μ_{rm}	1.066
Iron (M250-35A)	Stator tooth, apparent flux density (RFM), B_{sta}	1.8
	Stator bridges, flux density (TFM), B_{sb}	1.3
	Stator yoke, flux density, B_{sy}	1.1
	Rotor yoke, flux density, B_{ry}	1.3

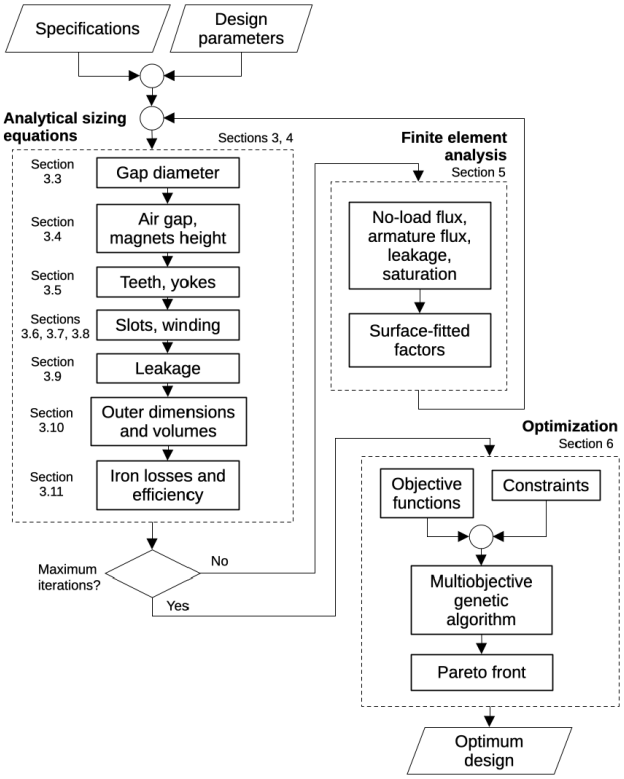

FIGURE 3. Flowchart of the sizing method and optimization.

of the flux density in different parts of the machines that have been taken in this work for calculations, based on the materials properties.

The no-load flux linkage and the inductances are key parameters for electrical machines sizing, as they are related to some important dimensions. The no-load flux linkage is proportional to the number of turns and the pole surface (1), (2). In classical electrical machines theory, the number of turns is related to the stator current and the gap diameter via the current load, that in this paper is defined as (14). Therefore, the torque (6) can be expressed as a function of the gap diameter, the pole length and the current load. If a geometrical ratio that relates the gap diameter and the pole length is defined, both magnitudes can be obtained. Besides, the d-axis inductance is inversely proportional to the d-axis air gap (15), so the d-axis air gap can be calculated once the number of turns is known. Therefore, in this first stage of the analytical design process it is shown that three outer parameters of the motor (torque, no-load flux linkage, inductance) can been correlated with three main dimensions (air gap diameter, pole length, air gap) using an intermediate parameter (the current load) to obtain the number of turns. In Section II-B the definitions of the no-load flux linkage for TFMs and RFMs will be discussed. Then the rest of the machine parameters can be obtained, according to the flowchart in Figure 3.

$$A_s = \frac{mN_{ms}I_s}{\pi D_g} \tag{14}$$

$$L_d \propto N_{ms}^2 g_d^{-1} \tag{15}$$

B. NO-LOAD FLUX LINKAGE AND D-AXIS ARMATURE FLUX LINKAGE

In PMSMs the energy conversion is produced by the interaction of the no-load flux linkage —created by the rotor PMs— and the armature flux linkage —created by the stator current flowing through the stator winding. Ideally, both fluxes cross entirely the air gap, thus being named ‘‘magnetizing’’ flux linkages. Actually, the stator currents produce an extra flux, i.e. the ‘‘leakage’’ flux, that does not cross the air gap but increases the inductance and contributes to magnetic saturation.

If the PMs or the stator coil are shortened β electrical degrees and the air gap is constant along the pole pitch, the flux density waveform in the air gap is rectangular [36], as shown in Figure 4. Only the radial component of the flux

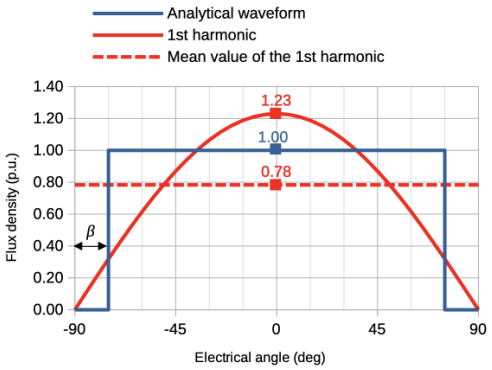

FIGURE 4. Rectangular flux density waveform assumed by the analytical model (solid blue line), its first harmonic (solid red line) and the mean value of the first harmonic (dashed red line).

density is assumed to contribute to flux, being constant along the axial direction. Assuming that the only reluctance of the magnetic circuit corresponds to the air gap (i.e. the machine is not saturated), the peak value of the no-load flux density (that is, the magnetic field created by PMs) is given by (16). On the other hand, the stator current in the q-axis produces a magnetomotive force (MMF) per pole $k_N N_{ms} \hat{I}_q$ along the q-axis air gap g_q, leading to a peak armature flux density in the q-axis named $\hat{B}_{aq}$ (17). N_{ms} is the number of turns per phase, so the equivalent turns factor k_N has been introduced as the ratio between the MMF per pole and the MMF per phase $N_{ms}\hat{I}_q$. Furthermore, similar magnitudes can be defined for the d-axis, based on the d-axis current $\hat{I}_d$.

$$\hat{B}_0 = \hat{B}_m \frac{k_{gma}}{1 + k_{gma}} \tag{16}$$

$$\hat{B}_{aq} = \frac{k_N N_{ms} \hat{I}_q}{g_q} \mu_o \tag{17}$$

The equivalent turns factor is defined in a different way for TFMs and RFMs, as stated in (18). In TFMs the armature field is created by a single-phase winding, as all the phases are axially stacked and so independent, and according to the Ampère's law (Figure 5a), the phase MMF $N_{ms}\hat{I}_q$ acts on each pole pair, the field crossing the air gap four times, that is why k_N turns out to be 1/4. On the other hand, in RFMs the field is created by the entire three-phase winding being fed by three-phase, balanced currents ($m = 3$), so the total MMF is $m/2$ times the MMF per phase. Moreover, as the number of turns per phase N_{ms} is $2p$ times the number of turns per pole, the MMF per phase has to be divided by $2p$ to obtain the MMF per pole, that is why k_N equals $m/(4p)$ in RFMs.

$$k_N = \begin{cases} 1/4 & \text{for TFMs} \\ m/(4p) & \text{for RFMs} \end{cases} \tag{18}$$

Once the peak values of the flux density are known, the amplitude of the first harmonics and their mean values are straightforward according to Fourier analysis (19), (20),

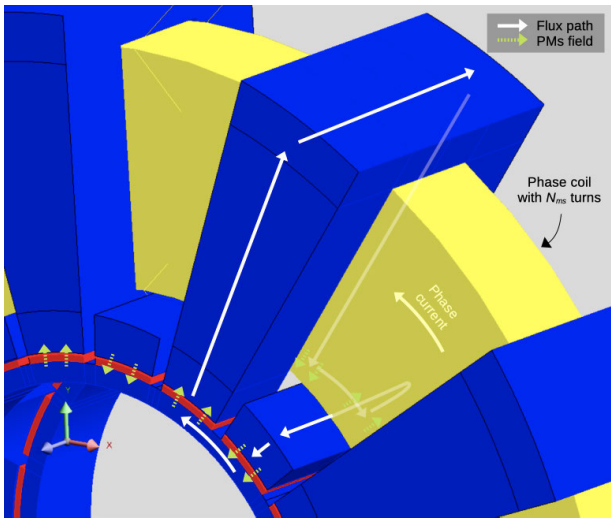

(a)

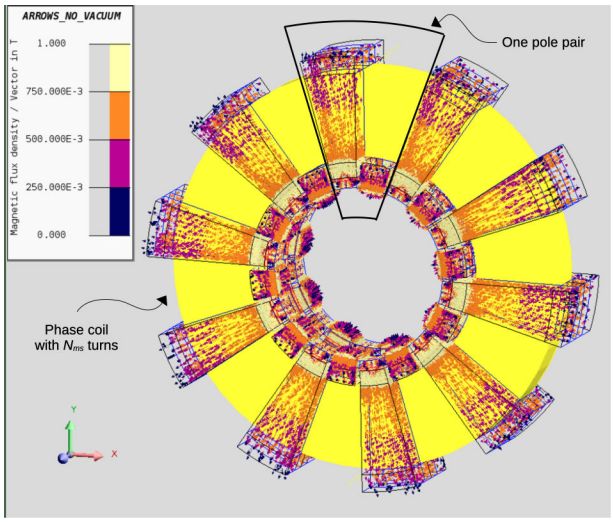

(b)

FIGURE 5. Ferromagnetic cores and coil in a TFM-U, single-phase view: (a) Illustration of the Ampère's Law in a single pole-pair, (b) Phase coil linking the flux of all pole pairs.

(21), (22). ξ_{r1} is the first-harmonic "winding" factor of the rotor (23) and ξ_{s1} is the stator first-harmonic winding factor, the latter defined as the product of the short-pitching factor and the distribution factor.

$$\hat{B}_{01} = k_{fr1}\hat{B}_0 = \frac{4}{\pi}\xi_{r1}\hat{B}_0 \tag{19}$$

$$\overline{B}_0 = \frac{2}{\pi}\hat{B}_{01} \tag{20}$$

$$\hat{B}_{aq1} = k_{fs1}\hat{B}_{aq} = \frac{4}{\pi}\xi_{s1}\hat{B}_{aq} \tag{21}$$

$$\overline{B}_{aq} = \frac{2}{\pi}\hat{B}_{aq1} \tag{22}$$

$$\xi_{r1} = \cos\beta = \cos\frac{180° - \alpha_r}{2} \tag{23}$$

In TFMs the magnetic flux circulates mainly through a plane that is perpendicular to the rotational plane, so the

magnetic and electrical loadings are decoupled. The phase coil is embraced by the flux of all the pole pairs at the same time, in a different way than RFMs, where each coil embraces the flux of a single pole pair and then the flux linkage per phase is obtained as the sum of all the pole pairs —if the coils are series-connected. In this case, the no-load and q-axis armature flux linkages follow (24) and (25) respectively for both TFM and RFMs. As the flux density has been reduced to its first harmonic, the flux linkage is assumed to be sinusoidal. Fringing, leakage or saturation effects can be included in the model using some factors, named no-load factor k_0, armature factor k_a, leakage factor k_σ and saturation factor k_{sat}. The leakage factor is further explained in Section II-I. Initially all these effects are neglected and in Section IV they will be analyzed via FEM.

$$\hat{\Psi}_0 = \begin{cases} \xi_{s1} N_{ms} \overline{B}_0 \tau_p l k_0 p & \text{for TFMs} \\ \xi_{s1} N_{ms} \overline{B}_0 \tau_p l k_0 & \text{for RFMs} \end{cases} \tag{24}$$

$$\hat{\Psi}_{aq} = \begin{cases} \xi_{s1} N_{ms} \overline{B}_{aq} \tau_p l \dfrac{k_{sat} k_a}{1 - k_\sigma} p & \text{for TFMs} \\ \xi_{s1} N_{ms} \overline{B}_{aq} \tau_p l \dfrac{k_{sat} k_a}{1 - k_\sigma} & \text{for RFMs} \end{cases} \tag{25}$$

C. D_G^3 SIZING EQUATION

As the no-load flux linkage is proportional to the pole surface, equations (1), (2), (6), (14) and (24) can be written as (26). In RFMs $D_g^2 l$ is the prismatic volume of the air gap, but not in TFMs as the pole length l is much lower than the outer length. Therefore, it is convenient to define a representative aspect ratio of each machine called "pole length factor" k_l as in (27). In this way, the number of pole pairs p that multiplies the no-load linkage of TFMs is canceled, so a common D_g^3 sizing equation can be deduced for TFMs and RFMs, as suggested in (28). If a "pole surface factor" (29) is defined to introduce the factor $\pi/2$ of TFMs, a common equation to calculate the gap diameter of TFMs and RFMs is deduced (30). Table 3 summarizes the main design parameters of the rotor and the stator that are needed to obtain the gap diameter.

$$T_1 \propto \begin{cases} A D_g^2 l p & \text{for TFMs} \\ A D_g^2 l & \text{for RFMs} \end{cases} \tag{26}$$

$$k_l = \begin{cases} \dfrac{l}{\tau_p} & \text{for TFMs} \\ \dfrac{l}{D_g} & \text{for RFMs} \end{cases} \tag{27}$$

$$T_1 \propto \begin{cases} A D_g^3 \dfrac{\pi}{2} k_l & \text{for TFMs} \\ A D_g^3 k_l & \text{for RFMs} \end{cases} \tag{28}$$

$$k_{Sp} = \begin{cases} \dfrac{\pi}{2} k_l & \text{for TFMs} \\ k_l & \text{for RFMs} \end{cases} \tag{29}$$

$$D_g = \sqrt[3]{\frac{T_1}{\pi \xi_{s1} \frac{k_{fr1} \hat{B}_0}{\sqrt{2}} A_s k_{Sp} k_0}} \tag{30}$$

TABLE 3. Rotor and stator design parameters.

	TFM	RFM
Magnets-to-air gap ratio, k_{gma}	3	
Carter factor	1	1.1
Rotor PMs span (electrical angle), α_r	150°	
Short-pitching of the stator winding	-	0°
Number of slots per pole and phase, q_s	-	1
Stator current load, A_s	From 10 to 40 kA/m	
Pole length factor, k_l	From 0.5 to 2.0	
No-load factor, k_0	1	
Armature factor, k_a	1	
Leakage factor, k_σ	0	
Saturation factor, k_{sat}	1	

D. AIR GAP AND MAGNETS RADIAL LENGTH

Once the gap diameter has been calculated, the equivalent gap length (31) can be obtained dividing (25) by (24), and substituting (11), (12), (14), (17), (19), (20), (21) and (22). In this way, both the no-load and armature flux specifications are fulfilled. Then the air gap and the PM's radial length are given by (4), (5).

$$g_d \simeq g_q = \frac{1}{\tan\varphi} \frac{\xi_{s1}}{\xi_{r1}} \frac{\mu_0}{\hat{B}_0} \frac{k_{sat}}{(1 - k_\sigma)} \frac{k_a}{k_0} k_N \frac{\pi\sqrt{2} A_s}{m} D_g \tag{31}$$

E. STATOR TEETH, STATOR YOKE, ROTOR YOKE AND TFM BRIDGES

In traditional electrical machines, copper or aluminum conductors are allocated in slots along the stator perimeter. TFMs do not have slots in the classical way, instead they have U-shaped cores that surround the winding —and sometimes I-shaped bridges— that guide the magnetic flux from one pole to another. Therefore, in TFMs the number of U-cores may resemble the number of slots in RFMs (32), as both serve to allocate the stator winding. Anyway, the number of slots and the slot pitch (33) are more relevant in RFMs, as these magnitudes are related to the winding factor and the stator tooth width (34), respectively. In TFMs it is more practical to impose the stator tooth width as a fraction k_s of the pole pitch, as the magnetic and electrical loadings are decoupled, and then calculate the apparent flux density in the stator tooth (35).

$$Q_s = \begin{cases} p & \text{for TFMs} \\ 2pmq_s & \text{for RFMs} \end{cases} \tag{32}$$

$$\tau_{Qs} = \frac{\pi D_g}{Q_s} = \frac{\tau_p}{m q_s} \quad \text{for RFMs} \tag{33}$$

$$w_{st} = \begin{cases} k_s \tau_p & \text{for TFMs} \\ \dfrac{\hat{B}_0}{B_{sta}} \tau_{Qs} & \text{for RFMs} \end{cases} \tag{34}$$

$$B_{sta} = \frac{\hat{B}_0 \tau_p}{w_{st}} \quad \text{for TFMs} \tag{35}$$

The dimensions of the stator yoke, the rotor yoke and the TFM bridges are determined from the no-load flux (36) applying the flux conservation law in the corresponding

TABLE 4. Winding design parameters.

Number of paths in parallel, a_s	1
Slot fill factor, k_{Cu}	0.4
Thermal constant, $A_s J_s$	120 kA/m·A/mm^2
Stator current density, J_s	From 12 to 3 A/mm^2
Slot width factor, k_{wss} (TFMs)	1.355

sections of the machines (37), (38), (39).

$$\hat{\Phi}_0 = \overline{B}_0 S_p \tag{36}$$

$$h_{sy} = \begin{cases} \dfrac{\hat{\Phi}_0}{B_{sy} l} = \dfrac{\overline{B}_0}{B_{sy}} \tau_p & \text{for TFMs} \\ \dfrac{\hat{\Phi}_0}{2B_{sy} l} = \dfrac{\overline{B}_0}{2B_{sy}} \tau_p & \text{for RFMs} \end{cases} \tag{37}$$

$$h_{ry} = \frac{\hat{\Phi}_0}{2B_{ry} l} = \frac{\overline{B}_0}{2B_{ry}} \tau_p \tag{38}$$

$$h_{sb} = \frac{\hat{\Phi}_0}{B_{sb} l} = \frac{\overline{B}_0}{B_{sb}} \tau_p \tag{39}$$

F. STATOR SLOTS

As in TFMs the U-cores embrace the hoop coil to guide the magnetic flux, they can be treated similarly to slots of conventional RFMs. RFMs have a distributed winding along the pole pairs in q_s slots per pole and phase, where q_s is not necessarily an integer number. Being N_{ms} the number of turns connected in series to produce flux linkages (24) and (25), obtained from current load (14), if the winding has a_s paths in parallel then the number of turns per slot (40) has to be increased proportionally.

$$N_{Qs} = \begin{cases} a_s N_{ms} & \text{for TFMs} \\ \dfrac{a_s}{q_s p} N_{ms} & \text{for RFMs} \end{cases} \tag{40}$$

If the RMS current density of each wire is J_s, the slot fill factor is k_{Cu} and the slot section is S_{ss}, the sum of currents through the slot section gives (41). Therefore, substituting (40) in (41) gives (42). The current density is a design parameter that is related to the thermal performance of the machine and will be explained in greater detail in Section II-H. Table 4 shows the main design parameters of the stator winding.

$$J_s k_{Cu} S_{ss} = N_{Qs} \frac{I_s}{a_s} \tag{41}$$

$$S_{ss} = \begin{cases} \dfrac{N_{ms} I_s}{k_{Cu} J_z} & \text{for TFMs} \\ \dfrac{N_{ms} I_s}{k_{Cu} J_z q_s p} & \text{for RFMs} \end{cases} \tag{42}$$

Equation (42) states that the cross-section of slots in RFMs is $q_s p$ times smaller than in TFMs for the same phase MMF, fill factor and current density. However, in RFMs the slot width is limited by the slot pitch and the stator tooth width, whereas in TFMs the conductors can be allocated freely along the axial direction (43). That is why it can be stated that in TFMs the magnetic and electrical loads (no-load flux linkage and current, respectively) do not compete for the same space. Moreover, as the slot height follows (44) and the slot section is imposed by previous design parameters, it is shown that in TFMs the slot width factor k_{wss} adjusts the slot aspect ratio k_{ss} (45), whereas in RFMs it is fixed by other parameters as the slot width cannot be adjusted freely. The slot width factor of TFMs is shown in Table 4 and it Section III-A it will be deduced as a function of the TFMs relative slot aspect ratio.

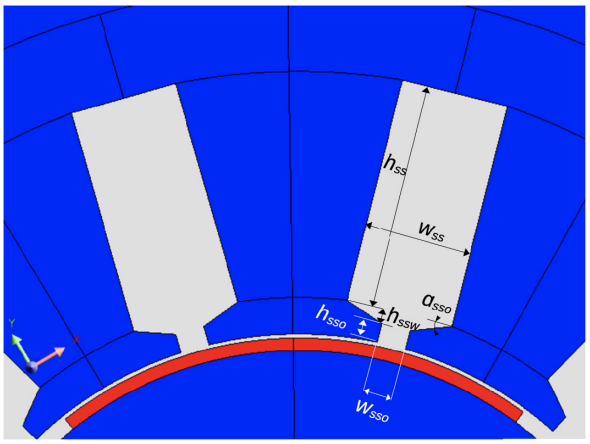

FIGURE 6. Slot dimensions in a RFM.

$$w_{ss} = \begin{cases} k_{wss} \tau_p & \text{for TFMs} \\ \tau_{Qs} - w_{st} = \dfrac{\left(1 - \hat{B}_0 / B_{sta}\right)}{m q_s} \tau_p & \text{for RFMs} \end{cases} \tag{43}$$

$$h_{ss} = \frac{S_{ss}}{w_{ss}} \tag{44}$$

$$k_{ss} = \frac{h_{ss}}{w_{ss}} \tag{45}$$

The slot opening width of the RFM (Figure 6) is calculated according to the Carter factor equation (46) given in [37]. The slot opening and the slot angle are $h_{sso} = 3$ mm and $\alpha_{sso} = 20°$, and thereby the slot wedge height follows (47).

$$w_{sso} = \frac{4}{3} \left(g_a + \tau_{Qs} - \frac{\tau_{Qs}}{k_C} \right) \tag{46}$$

$$h_{ssw} = \frac{w_{ss} - w_{sso}}{2} \tan \alpha_{sso} \tag{47}$$

G. WINDING LENGTH AND RESISTANCE

In electrical machines the winding is usually divided into active winding and end-winding. The active winding is located into the stator slots, whereas the end-winding serves as a connection between active coil sides. In conventional RFMs, the end-winding has a straight part along the axial direction (length l_{we}) and a curved part (length w_{we}). Furthermore, the end-winding length can be reduced using short-pitched coils or a fractional number of slots per pole and phase q_s. However, in TFMs the end-winding length is fixed

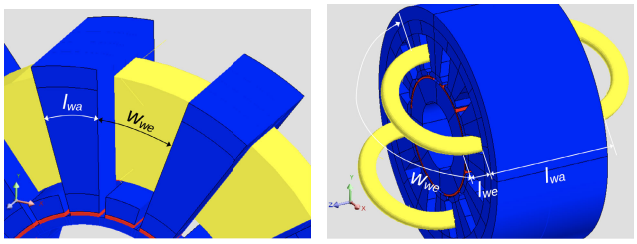

(a) (b)

FIGURE 7. Winding lengths in the finite element model, active (wa) and end-winding (we): (a) TFM-U, (b) RFM.

by the machine dimensions as the phase coil is not distributed in slots. Figure 7 illustrates active and end-winding lengths of TFMs and RFMs, given by (48), (49) and (50). The sign ± should be taken as positive if the stator is external (as in this work), and negative otherwise. Then the total length of one turn can be calculated (51), and thereby the phase resistance (52).

$$l_{wa} = \begin{cases} \dfrac{\pi k_s}{p}\left[D_g/2 \pm (g_a/2 + h_{sb} + h_{ss}/2)\right] & \text{for TFMs} \\ l & \text{for RFMs} \end{cases} \tag{48}$$

$$l_{we} = \begin{cases} 0 & \text{for TFMs} \\ 1\text{ mm} & \text{for RFMs} \end{cases} \tag{49}$$

$$w_{we} = \begin{cases} \dfrac{\pi\,[1+(1-k_s)]}{p}\left[D_g/2 \pm (g_a/2 + h_{sb} + h_{ss}/2)\right] \\ \quad \text{for TFMs} \\ \pi\left[D_g/2 \pm (g_a/2 + h_{sso} + h_{ssw} + h_{ss}/2)\right]\sin\left(\dfrac{\pi/2}{p}\right) \\ \quad \text{for RFMs with } q_s = 1 \end{cases} \tag{50}$$

$$l_{Ns} = \begin{cases} p\,(l_{wa} + w_{we}) & \text{for TFMs} \\ 2\,(l_{wa} + 2l_{we} + w_{we}) & \text{for RFMs} \end{cases} \tag{51}$$

$$R_{ms} = \frac{1}{a_s}\rho_{Cu}\frac{N_{ms}l_{Ns}}{k_{Cu}S_{ss}/N_{Qs}} \tag{52}$$

H. CURRENT DENSITY AND THERMAL EQUATION

If iron, mechanical and stray losses are neglected against copper losses P_{Cu}, the temperature rise follows (53), being R_{th} the thermal resistance of the stator housing. D_o and l_o are the outer dimensions of the machine and α_{th} is the heat transfer coefficient. Copper losses are given by (54) substituting (41) and (52). Therefore, a comprehensive equation of the temperature rise (55) can be written if the current load definition is used (14). It is stated that the thermal constant A_sJ_s is of great importance for the machine thermal performance, then if the current load is increased, the current density must be decreased in order to not overheat the windings. As the heat transfer coefficient cannot be determined accurately without specific FEM or experimental validation, provided that typical values are not available in the literature, only the thermal constant values of literature [38] can be considered in the design process. The current load values were given in Table 3, so Table 4 gives the thermal constant and current density values that have been taken in this work. The thermal constant is the same for all the machines analyzed here as all of them are intended for the same cooling requirements.

$$\Delta T = P_{Cu}R_{th} = \frac{P_{Cu}}{\alpha_{th}\pi D_o l_o} \tag{53}$$

$$P_{Cu} = mR_{ms}I_s^2 = m\rho_{Cu}l_{Ns}J_sN_{ms}I_s \tag{54}$$

$$\Delta T = \frac{\rho_{Cu}}{\alpha_{th}}\frac{l_{Ns}}{l_o}\frac{D_g}{D_o}A_sJ_s \tag{55}$$

I. INDUCTANCES

As PMSMs have magnets in the rotor, only the stator self-inductances are defined. The flux linkage produced by the stator current is usually divided into magnetizing flux and leakage flux, and so the inductance (56), (57). As d- and q-axis inductances are equal in S-PMSMs, they are interchangeable here. The leakage factor is defined as (58), so the highest the leakage in an electrical machine, the highest the leakage factor. Initially leakage was neglected in the machine sizing (Table 3). As the total inductance is given by the motor requirements (Table 1), an increase in the leakage factor would increase the d-axis gap in order to reduce the magnetizing inductance (31), thus increasing the air gap and the PMs height (4), (5).

$$L_q = L_\sigma + L_{qm} \tag{56}$$

$$L_{qm} = \frac{\hat{\psi}_{aq}}{\hat{I}_q} \tag{57}$$

$$k_\sigma = \frac{L_\sigma}{L_q} \tag{58}$$

The leakage inductance L_σ is given by (59). Factors $\frac{p}{a_s}$ and $\frac{2q_sp}{a_s}$ are the number of series-connected slots in TFMs and RFMs, respectively. λ is the specific permeance of each component of the flux linkage (Table 5), referred to the pole pitch in case of TFMs and to the pole length in RFMs, as they are the ''slot depths'' along which the conductors are located.

$$L_\sigma = \begin{cases} \dfrac{p}{a_s}N_{Qs}^2\mu_0\tau_p\sum\lambda & \text{for TFMs} \\ \dfrac{2q_sp}{a_s}N_{Qs}^2\mu_0 l\sum\lambda & \text{for RFMs} \end{cases} \tag{59}$$

As in TFMs the ''slot depth'' (i.e. the tooth width) depends on the radius, from w_{st1} in the stator bridge to w_{st2} in the stator yoke, the proposed formulae for the slot leakage permeances (60), (61) include this variation. A negative sign in the expression of $w_{st}(h)$ must be taken in case of an external stator. Expressions of the end-winding and tooth tip leakage

TABLE 5. Specific leakage permeances.

	TFM-U	RFM
λ_{ss}	$\frac{w_{st2}}{\tau_p}\frac{h_{ss}}{3w_{ss}} - \frac{\pi k_s}{p}\frac{h_{ss}}{\tau_p}\frac{h_{ss}}{4w_{ss}}$	$\frac{h_{ss}}{3w_{ss}}$
λ_{ssw}	0	$\frac{h_{ssw}}{(w_{ss}+w_{sso})/2}$
λ_{sso}	$\frac{w_{st1}}{\tau_p}\frac{h_{sb}}{w_{ss}} - \frac{\pi k_s}{p}\frac{h_{sb}}{\tau_p}\frac{h_{sb}}{2w_{ss}}$	$\frac{h_{sso}}{w_{sso}}$
λ_{ew}	$\frac{0.3q_s w_{we}}{\tau_p}$	$\frac{0.3q_s(2l_{we}+w_{we})}{l}$
λ_{sb}	$\frac{4h_{sb}}{\tau_p - w_{st}}\frac{l}{\tau_p}$	0
λ_{tt}	0	$\frac{g_a}{w_{sso}+0.8g_a}$

have been taken from [38] and [39], respectively.

$$N_{Qs}^2\tau_p\lambda_{ss} = \int N_{Qs}^2(h)\frac{w_{st}(h)}{w_{ss}}\mathrm{d}h$$
$$\text{with}\quad N_{Qs}(h) = N_{Qs}\frac{h}{h_{ss}}\ ,$$
$$w_{st}(h) = \left(w_{st2} \mp h\frac{\pi k_s}{p}\right) \tag{60}$$

$$N_{Qs}^2\tau_p\lambda_{sso} = \int N_{Qs}^2\frac{w_{st}(h)}{w_{ss}}\mathrm{d}h$$
$$\text{with}\quad w_{st}(h) = \left(w_{st1} \mp h\frac{\pi k_s}{p}\right) \tag{61}$$

J. OUTER DIMENSIONS AND VOLUMES

Hitherto, there is no big difference when it comes to designing an electrical machine with an external or internal stator. As long as there is enough space to allocate the stator in the inner part of the machine, only a few signs must be changed when calculating the winding lengths and the slot specific permeance. The major differences when choosing an external or internal stator lay on the outer diameter, as the rotor radial height is usually lower than the stator height. The expressions for the inner diameter, outer diameter, phase length and outer length in the external stator case are given in (62), (63), (64), (65). Furthermore, it should be noted that the outer length of TFMs is proportional to the number of phases, as they are generally stacked in the axial direction. The outer-length-to-outer-diameter ratio k_{loDo} (66) is of importance as is determines the true aspect ratio of the machine. Once the outer dimensions have been determined, any volumes and masses can be calculated. In this work the mass of active materials m_a, that is, the sum of copper, iron and PMs (67), has been taken as the reference to determine the torque density.

$$D_i = D_g - \left(g_a + 2g_m + 2h_{ry}\right) \tag{62}$$

$$D_o = \begin{cases} D_g + \left(g_a + 2h_{sb} + 2h_{ss} + 2h_{sy}\right) \\ \text{for TFMs} \\ D_g + \left(g_a + 2h_{sso} + 2h_{ssw} + 2h_{ss} + 2h_{sy}\right) \\ \text{for RFMs} \end{cases} \tag{63}$$

$$l_m = \begin{cases} 2l + w_{ss} & \text{for TFMs} \\ l & \text{for RFMs} \end{cases} \tag{64}$$

$$l_o = \begin{cases} ml_m & \text{for TFMs} \\ l_m & \text{for RFMs} \end{cases} \tag{65}$$

$$k_{loDo} = \frac{l_o}{D_o} \tag{66}$$

$$m_a = d_{Fe}\left(V_{st} + V_{sy} + V_{ry} + V_{sb}\right) + d_m V_m + d_{Cu}V_{Cu} \tag{67}$$

K. IRON LOSSES AND EFFICIENCY

As the volumes of each part of the machine can be determined, the Steinmetz formula gives iron losses (68). In this work the specific, rated losses of M250-35A electrical steel have been used in the Steinmetz formula, as the iron losses coefficients of the material were not available. Finally, the efficiency of the machine can be calculated with (69), having neglected mechanical and stray losses.

$$P_{Fe1} = \frac{2.5\,\mathrm{W/kg}}{1.5^2\cdot 50\,\mathrm{T^2Hz}}d_{Fe}\frac{\omega_1}{2\pi}\cdot \cdot\left(B_{sta}^2V_{st} + B_{sy}^2V_{sy} + B_{ry}^2V_{ry} + B_{sb}^2V_{sb}\right) \tag{68}$$

$$\eta = \frac{T_1\frac{2\pi}{60}n_1}{T_1\frac{2\pi}{60}n_1 + P_{Cu} + P_{Fe1}} \tag{69}$$

III. SIMILARITY EQUATIONS AND PARAMETRIC STUDY

The analytical sizing method presented in this work allows to compare TFMs and RFMs, given the specifications and the same design parameters for both topologies, using the similarity equations. Furthermore, the main dimensions depend on the current load in a similar way both in TFMs and RFMs. These analyses are presented in Section III-A and Section III-B, respectively.

A. SIMILARITY EQUATIONS

According with the proposed analytical sizing method and the design parameters given in Table 1, Table 2, Table 3 and Table 4, the main dimensions of TFMs and RFMs can be compared defining some dimensionless numbers that represent the TFM dimensions with respect to the RFM dimensions (70), (71), (72), (73), (74), (75). In the definition of the relative PMs volume, $2p^*m^{(T)}$ is the relative number of PMs: TFMs have 4 magnets per pole pair and $m^{(T)}$ stacks (one per phase), whereas RFMs have 2 PMs per pole pair and a single-stack. Results are shown in Table 6. For the same torque, no-load flux density, current load and pole length factor, the diameter of a TFM is 0.86 times the diameter of a RFM. Moreover, it should be noted that the PMs volume of the TFM is less than half when compared with the RFM. An increase in the TFM pole pairs would lead to a further reduction in the relative pole pitch and the relative pole length, and so the PMs volume.

$$D_g^* = \sqrt[3]{\frac{1}{k_{Sp}^*}},\quad k_{Sp}^* = \frac{\pi}{2},\quad \tau_p^* = \frac{D_g^*}{p^*} \tag{70}$$

$$l^* = \frac{\pi}{2p^{(T)}}D_g^* \tag{71}$$

TABLE 6. Relative dimensions of TFMs with respect to RFMs in this work.

Gap diameter, D_g^*	0.86
Number of pole pairs, p^*	5
Pole pitch, τ_p^*	0.17
Pole length, l^*	0.14
d- and q-axis gap, $g_d^* = g_q^*$	0.57
Air gap and PMs height, $g_a^* = g_m^*$	0.63
Stator yoke, h_{sy}^*	0.34
Rotor yoke, h_{ry}^*	0.17
Slot section, S_{ss}^*	1.72
Slot aspect ratio, k_{ss}^*	1
Slot width, w_{ss}^*	1.31
Slot height, h_{ss}^*	1.31
PMs volume, V_m^*	0.44

$$g_d^* = g_q^* = k_N^* D_g^* = \frac{p^{(R)}}{m^{(R)}} D_g^*, \quad g_a^* = g_m^* = \frac{g_d^*}{k_C^*} \tag{72}$$

$$h_{sy}^* = 2\tau_p^*, \quad h_{ry}^* = \tau_p^* \tag{73}$$

$$S_{ss}^* = D_g^* p^{(R)} q^{(R)}, \quad w_{ss}^* = \sqrt{\frac{S_{ss}^*}{k_{ss}^*}}, \quad h_{ss}^* = k_{ss}^* w_{ss}^* \tag{74}$$

$$V_m^* = 2m^{(T)} D_g^* g_m^* l^* \tag{75}$$

It should be noted that the relative slot aspect ratio k_{ss}^* can be chosen freely, as an additional degree of freedom in TFMs design that results from the decoupling of the magnetic and electric loadings. In this work, unit relative slot aspect ratio has been chosen for the parametric study, and then in the optimization stage is it changed to a design variable. Thereby, the expression of the stator slot width factor k_{wss} in (43) as a function of the design parameters can be deduced from the similarity equations presented here, as shown in (76), (77).

$$w_{ss}^{(T)} = \sqrt{\frac{S_{ss}^*}{k_{ss}^*}} w_{ss}^{(R)} = \sqrt{\frac{D_g^* p^{(R)} q^{(R)}}{k_{ss}^*}} \frac{\left(1 - \hat{B}_0 / B_{sta}^{(R)}\right)}{m^{(R)} q_s^{(R)}} \frac{\tau_p^{(T)}}{\tau_p^*} \tag{76}$$

$$k_{wss}^{(T)} = \sqrt{\frac{p^*}{D_g^* k_{ss}^*} \frac{p^{(T)}}{q_s^{(R)}}} \frac{\left(1 - \hat{B}_0 / B_{sta}^{(R)}\right)}{m^{(R)}} \tag{77}$$

Hitherto the relative dimensions do not depend on the current load or the pole length ratio. The relative outer length (78) and the relative rotor volume (79) depend both on TFM and RFM parameters, but their comparison is quite straightforward. For the values presented in the parametric study (unit relative aspect ratio, RFM pole length factor from 0.5 to 2), the relative outer length and the relative rotor volume are presented in Table 7. Although the TFMs diameter is lower according to Table 6, in some cases they have a bulky rotor regarding the axial length when compared with RFMs. However, their rotor and stator yokes are much smaller, so anyway they can take advantage in terms of the active mass.

$$l_o^* = m^{(T)} \left(2l^* + \frac{k_{wss}^{(T)}}{k_l^{(R)}} \frac{\pi}{2p^{(T)}} D_g^* \right) \tag{78}$$

$$V_r^* = {D_g^*}^2 l_o^* \tag{79}$$

TABLE 7. Relative outer length and rotor volume for different RFMs pole length factor.

Pole length factor, RFM $k_l^{(R)}$	0.5	1	1.5	2
Outer length, l_o^*	1.91	1.36	1.18	1.09
Rotor volume, V_r^*	1.41	1.01	0.87	0.80

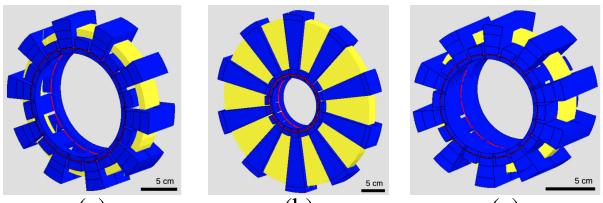

FIGURE 8. TFM geometries (single-phase views) for: (a) $k_l = 0.5$, $A_s = 10$ kA/m, (b) $k_l = 0.5$, $A_s = 30$ kA/m, (c) $k_l = 2.0$, $A_s = 10$ kA/m.

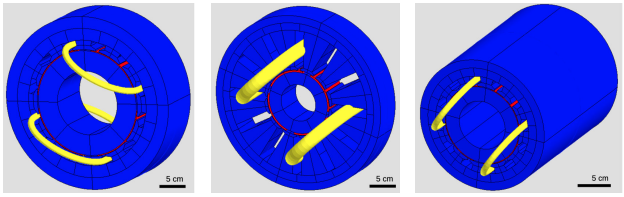

FIGURE 9. RFM geometries for: (a) $k_l = 0.5$, $A_s = 10$ kA/m, (b) $k_l = 0.5$, $A_s = 30$ kA/m, (c) $k_l = 2.0$, $A_s = 10$ kA/m.

Figure 8 and Figure 9 show some TFMs and RFMs that result from the analytical sizing method presented here. It is shown that the current load has a great impact on the gap diameter and specially on the slot height. Therefore Section III-B analyzes the dependance of the main dimensions with the current load.

B. PARAMETRIC STUDY

The D_g^3 equation (30) states that the current load and the pole length ratio are key parameters in electrical machines sizing, as the rest of the parameters are given by the specifications or minor design constraints. Therefore, in this section a parametric study will be conducted with respect to the current load for various pole length ratios, both for TFMs and RFMs.

The proposed analytical model allows to write the main dimensions of the machines as power functions of the current load. The gap diameter, the pole pitch and the pole length are a decreasing function with the current load (80), see Figure 10. The tooth width and the yokes' heigths have the same dependance as they are proportional to the pole pitch. The air gap and the magnets height increase with current load (81), Figure 11. Furthermore, according to (82) the stator slot section increases with the current load at the same that the slot width decreases, thus resulting in a steep increase of the slot height and the slot aspect ratio. Although the outer length of TFMs depends on the additional degree of freedom related to the slot aspect ratio, with the proposed analytical model it can be written as proportional to the pole pitch, so

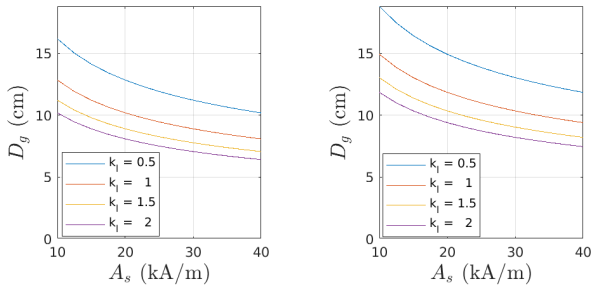

FIGURE 10. Gap diameter, parametric study: (a) TFM-U, (b) RFM.

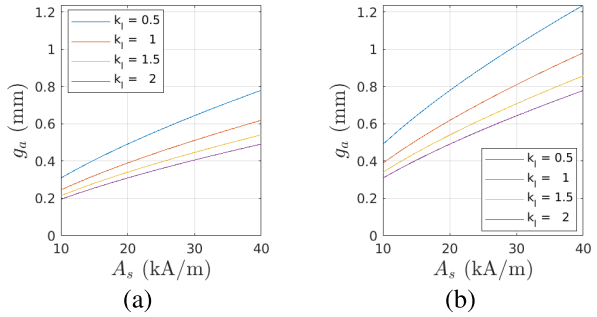

FIGURE 11. Air gap length, parametric study: (a) TFM-U, (b) RFM.

it follows the same dependance as the diameter (Figure 12). Moreover, neglecting the air gap and the slot opening against the outer diameter, it is shown that the outer diameter and the outer volume have a global minimum (83), as shown in Figure 13 and Figure 14 (here the torque density has been depicted, so it has a global maximum). The torque density with respect to the active mass follows a similar dependance, according to Figure 15.

$$D_g,\ \tau_p,\ l,\ w_{st},\ h_{sy},\ h_{ry},\ h_{sb} \propto A^{-1/3} \tag{80}$$

$$g_d,\ g_q,\ g_a,\ g_m \propto A^{2/3} \tag{81}$$

$$S_{ss} \propto A^{5/3}, \quad w_{ss} \propto A^{-1/3}, \quad h_{ss} \propto A^2, \quad k_{ss} \propto A^{7/3} \tag{82}$$

$$l_o \propto A^{-1/3}, \quad D_o \propto aA^{-1/3} + bA^2, \quad V_o \propto a'A^{-1} + b'A^{11/3} + c'A^{4/3} \tag{83}$$

An insight into Table 8 and Table 9 shows that leakage flux of TFMs seems to be much higher than RFMs. Furthermore, the leakage flux through the stator bridges is by far the biggest contribution to leakage in TFMs, and both in the TFM and RFM the slot leakage flux increases a lot with the current load: according to Table 5 it is proportional to h_{ss}/w_{ss} and therefore to $A^{7/3}$ (82).

IV. FINITE ELEMENT ANALYSIS

In order to validate the analytical model, finite element simulations have been conducted using Altair Flux3D software. In TFMs, 3D geometries become mandatory for finite element modeling as their flux path is inherently three-dimensional, whereas in RFMs 3D models are not essential,

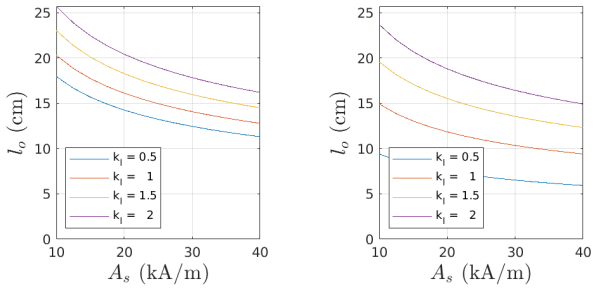

FIGURE 12. Outer length, parametric study: (a) TFM-U, (b) RFM.

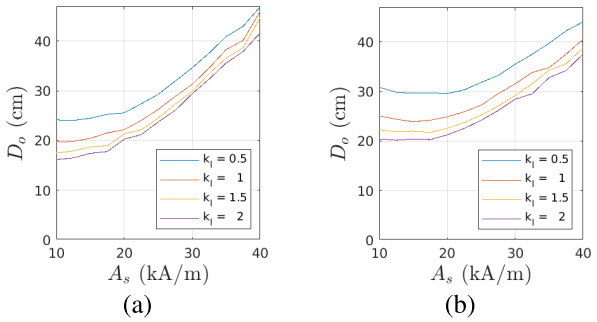

FIGURE 13. Outer diameter, parametric study: (a) TFM-U, (b) RFM.

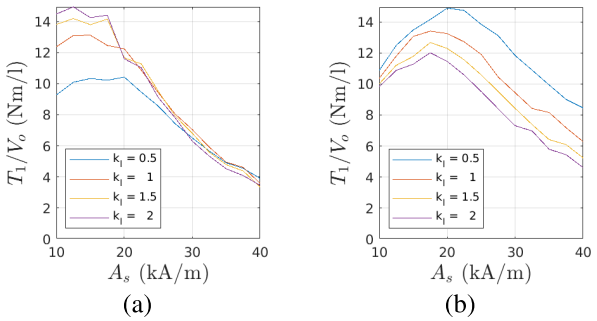

FIGURE 14. Torque density with respect to the outer volume, parametric study: (a) TFM-U, (b) RFM.

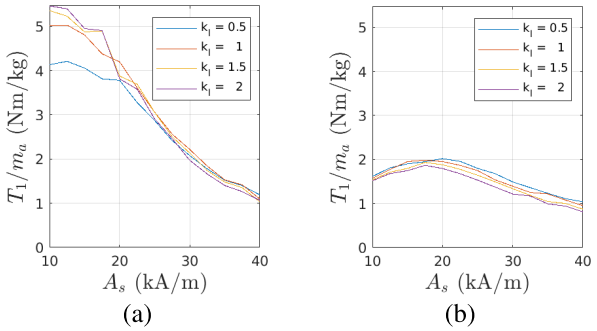

FIGURE 15. Torque density with respect to the active mass, parametric study: (a) TFM-U, (b) RFM.

but convenient if 3D effects such as the end-winding leakage flux and the fringing flux at the machine end have to be

TABLE 8. Specific leakage permeances and leakage factor in TFMs with $k_I = 1$.

A_s(kA/m)	10	20	30	40
λ_{ew}	0.4384	0.5517	0.7858	1.1656
λ_{sb}	12.1417	12.1417	12.1417	12.1417
λ_{ss}	0.1442	0.7387	2.4037	6.3471
λ_{sso}	0.3364	0.3370	0.3376	0.3382
λ_{ssw}	0	0	0	0
λ_{tt}	0	0	0	0
k_σ	0.7496	0.8582	0.9029	0.9280

TABLE 9. Specific leakage permeances and leakage factor in RFMs with $k_I = 1$.

A_s(kA/m)	10	20	30	40
λ_{ew}	0.3821	0.4595	0.6194	0.8316
λ_{sb}	0	0	0	0
λ_{ss}	0.1542	0.6425	1.7641	3.2639
λ_{sso}	0.5707	0.6544	0.6873	0.6989
λ_{ssw}	0.2174	0.2060	0.1951	0.1847
λ_{tt}	0.0699	0.1216	0.1615	0.1932
k_σ	0.0630	0.1753	0.3306	0.5148

included in computations. Figure 16 shows the 3D meshed models, together with the boundary conditions implemented in Flux3D software. A second-order, extruded mesh has been used to improve the accuracy and reduce the computation time. It should be noted that only half of the axial length has been modeled both in the TFM and RFM cases, but using different symmetry and periodicity boundary conditions. In the TFM-U (but not in other TFMs) the magnetic field is normal to the middle cross-section plane, whereas in RFMs the magnetic field is tangent and so confined in the middle cross-section plane. Besides, as TFMs geometry is different in the north and south poles, cyclic boundary conditions must be used instead of the anticyclic boundary condition typically applied in RFMs. Furthermore, the magnetic field is assumed to be zero in infinity by use of an infinite box technique. Initially, constant magnetic permeability of iron has been assumed in order to compare the FEM results with the analytical model —based on a linear material. In Subsection IV-B3 the influence of magnetic saturation has been quantified separately.

According to Figure 4, in the analytical sizing equations the radial air gap flux density is reduced to its first harmonic, and so the flux linkages and voltages, neglecting any 3D or higher-order-harmonic effects. Furthermore, in (16), (17) it is assumed that the only reluctance in the magnetic circuit corresponds to the equivalent air gap (PMs + air gap), with no leakage or fringing effects. Therefore, in this work analytical and FEM models have been compared in order to validate previous assumptions. For this purpose, two factors have been defined, both for the no-load flux and the q-axis armature flux, named "FEM no-load factor" and "FEM armature factor". At the same time, each factor is the product of the "FEM peak factor", the "FEM form factor" and the "FEM flux factor", and each of these three factors can be calculated dividing the FEM quantities by the analytical magnitudes. For instance, in case of the no-load flux the peak, form

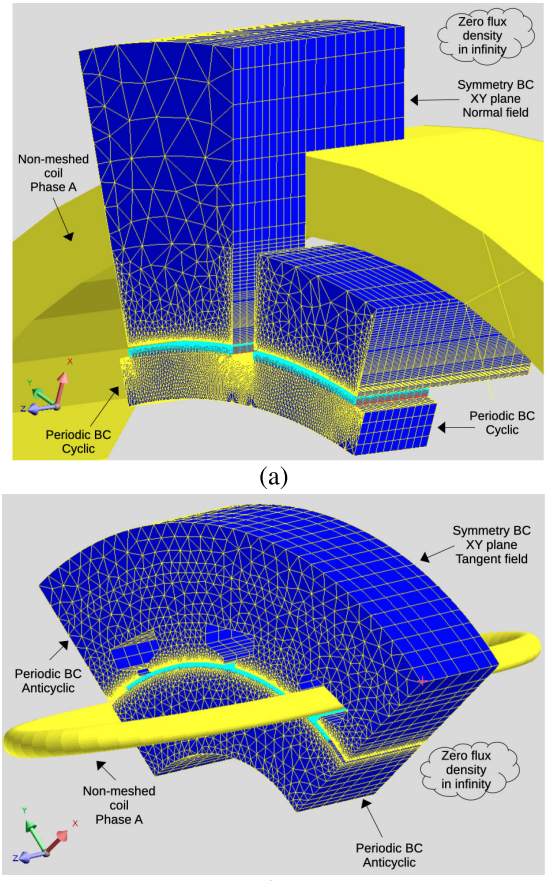

FIGURE 16. 3D FEM meshed models and boundary conditions (BC), having removed the surrounding air: (a) TFM-U with $k_I = 0.5$, $A_s = 10$ kA/m, (b) RFM with $k_I = 0.5$, $A_s = 10$ kA/m.

and flux factors follow (85), (86) and (87), respectively, their denominators being given by (16), (19), (20), (24). The definitions in case of the q-axis armature flux are analogous, but using the armature field (17), (21), (22) and flux (25). It should be noted that the proposed peak and form factors are based exclusively on the air gap flux density waveform, whereas the flux factor takes into account other effects related to flux (such as leakage and fringing) that affect its first harmonic amplitude even though the mean value of the air gap flux density is perfectly known. Ultimately both the no-load flux factor and the armature flux factor can be correlated with the machine design parameters via surface fitting (88) and later re-used to improve the accuracy of the machine sizing method. In this work, the 'poly23' algorithm from MATLAB has been to determine coefficients a_{ii} in (88).

$$k_0 = k_{0pk} k_{0f} k_{0\Psi}, \quad k_a = k_{apk} k_{af} k_{a\Psi} \tag{84}$$

$$k_{0pk} = \frac{\hat{B}_0^{(FEM)}}{\hat{B}_0^{(analytical)}} \tag{85}$$

$$k_{0f} = \frac{\overline{B}_0^{(FEM)} / \hat{B}_0^{(FEM)}}{\overline{B}_0^{(analytical)} / \hat{B}_0^{(analytical)}} \tag{86}$$

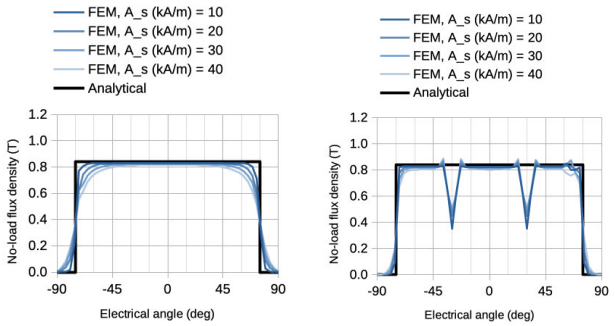

FIGURE 17. FEM no-load radial flux density: (a) TFM-U with $k_l = 1$, (b) RFM with $k_l = 1$.

$$k_{0\Psi} = \frac{\Psi_{01}^{(FEM)}/\overline{B}_0^{(FEM)}}{\Psi_{01}^{(analytical)}/\overline{B}_0^{(analytical)}} \tag{87}$$

$$\begin{aligned} f(k_l, A_s) = {} & a_{00} + a_{10}k_l + a_{01}A_s + a_{20}k_l^2 \\ & + a_{11}k_lA_s + a_{02}A_s^2 \\ & + a_{21}k_l^2A_s + a_{12}k_lA_s^2 + a_{03}A_s^3 \end{aligned} \tag{88}$$

A. NO-LOAD FLUX

Firstly the no-load flux density waveform has been obtained for each TFM and RFM with a static FEM simulation (active PMs but no stator current in a fixed rotor position), and then the first harmonic of the flux linkage has been determined with a multistatic simulation and subsequent Fourier data analysis. Figure 17 illustrates the no-load radial flux density in the air gap for those machines with $k_l = 1$, where the zero electrical angle corresponds to the rotor d-axis being aligned with the stator A-phase. It is shown that the peak values obtained via FEM match the analytical results, however, the no-load flux density waveforms of the TFM seem to be smoother than its RFM counterparts —thus altering the form factor— specially when the current load increases (so the gap diameter decreases). In Figure 18 two field maps have been depicted in the middle cross-section of the rotor PMs. Regarding the arrows density, it can be stated qualitatively that the TFM under analysis exhibits higher PMs leakage flux and higher air gap fringing flux than the RFM. This effect could be explained by the fact that in the TFM the rotor inter-pole air space lays entirely under the stator inter-pole air space (Figure 18a), so the air gap reluctance starts to increase at the same time that the PMs flux density starts to decrease near the contact surface between PMs and air. However, in the RFM the rotor inter-pole air space lays mostly under the stator tooth tip (Figure 18b), so the reluctance does not change on the stator side, leading to a steeper decrease in the air gap flux density. In this work the stator tooth width equals the PMs span in all the TFMs, but changing this ratio would probably make the no-load flux density waveform to be more rectangular or more sinusoidal.

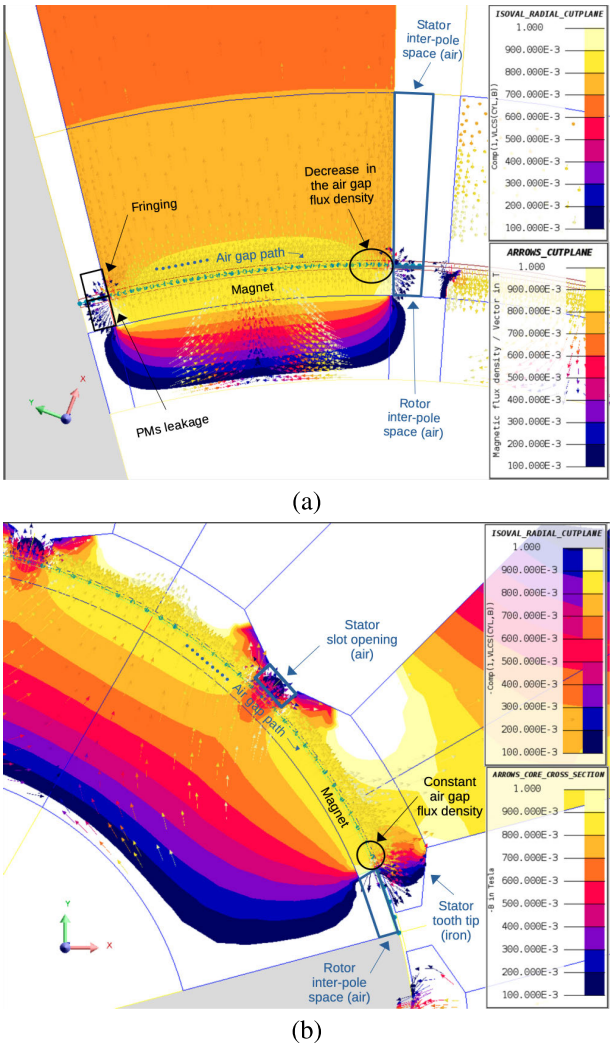

FIGURE 18. FEM no-load radial flux density (colormaps) and no-load flux density (arrows): (a) TFM-U with $k_l = 1$, $A_s = 20$ kA/m (b) RFM with $k_l = 1$, $A_s = 20$ kA/m.

Figure 19 shows the no-load factor or the TFMs and RFMs that have been designed in this work. The no-load factor is close to one in most cases, thus proving the accuracy of the analytical method, but it seems to decrease with the current load both in the TFMs and RFMs. Figure 20 depicts the no-load factor decomposition for those machines with $k_l = 1$. According to the results, the contributions of the no-load factor do not change significantly with the current load, so the decrease in the no-load factor can be attributed equally to the peak factor, the form factor and the flux factor.

B. Q-AXIS ARMATURE FLUX

The armature flux is usually divided into magnetizing flux and leakage flux when designing electrical machines — as the inductance, according to (56)—, so it has been analyzed separately via the armature factor and the leakage factor (linear material) in Subsections IV-B1 and IV-B2,

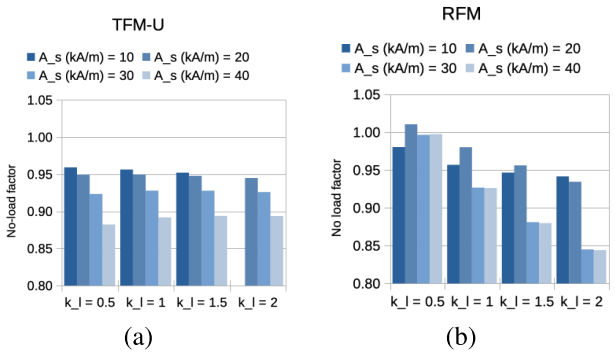

FIGURE 19. FEM no-load factor: (a) TFM-U, (b) RFM.

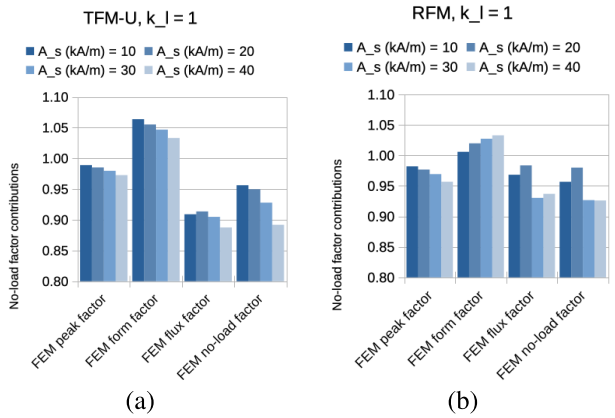

FIGURE 20. Contributions to the FEM no-load factor: (a) TFM-U with $k_l = 1$, (b) RFM with $k_l = 1$.

and then the effect of saturation has been analyzed in Subsection IV-B3.

1) ARMATURE FACTOR

Figure 21 depicts the armature flux waveforms in the q-axis for those machines with $k_l = 1$. It is clearly shown that the FEM waveforms differ from the analytical assumptions. In the TFMs the air gap armature flux density seems to concentrate around the stator tooth corners and then it decreases to zero with a certain slope, and the same occurs in the RFMs near the slot openings, but in case of the RFM the peak values of the flux density are also higher than the expected by the analytical calculations. An insight into the FEM field maps (Figure 22) shows that the TFM exhibits some leakage flux coming from the stator bridges and fringing flux in the rotor inter-pole space that explains the increase of the armature flux density near the stator tooth corners. Besides, the RFM seems to suffer from flux concentration in the top part of the stator tooth tip, i.e. the smallest cross-section are in the magnetic circuit, and this could be behind the higher peak value of the flux density.

According to Figure 23a, in the TFMs the armature factor increases with the current load, and this increase is mainly determined by the form factor according to

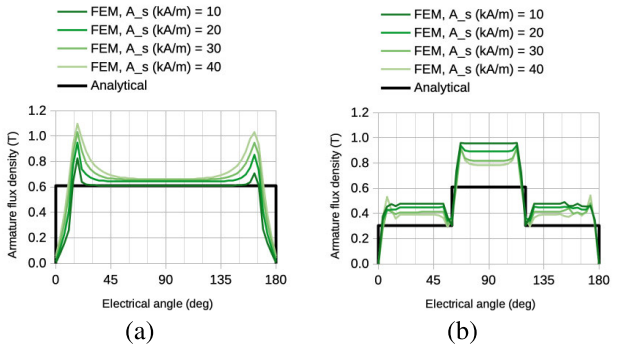

FIGURE 21. FEM armature flux density: (a) TFM-U with $k_l = 1$, (b) RFM with $k_l = 1$.

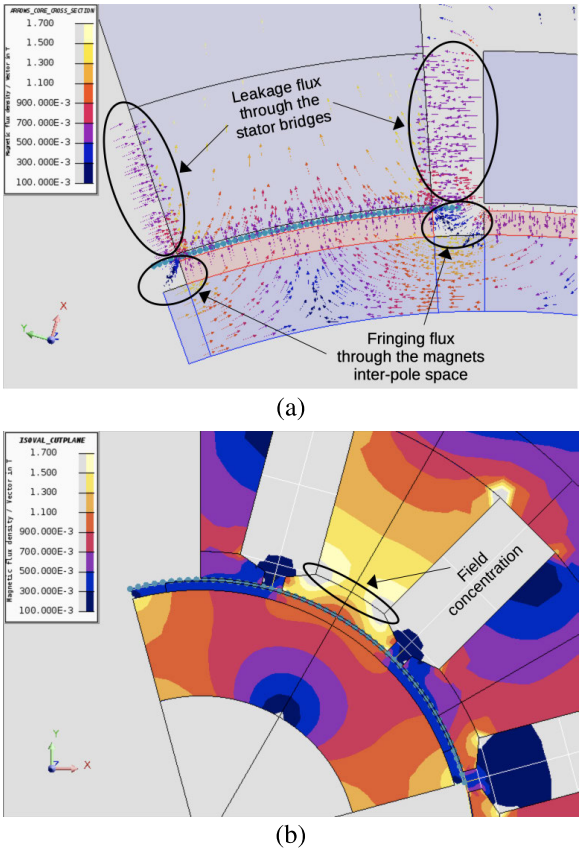

FIGURE 22. FEM armature flux density: (a) leakage and fringing fluxes in the TFM-U with $A_s = 20$ kA/m, $k_l = 1$, (b) non-uniform field in the RFM with $A_s = 20$ kA/m, $k_l = 1$.

Figure 24a. In case of RFMs (Figure 23b), the changes in the armature factor are determined by the peak factor, as the form and flux factors do not change with the current load (Figure 24b).

2) LEAKAGE FACTOR

The leakage inductance and so the leakage factor k_σ can be deduced from finite element simulations using (56), as the magnetizing fluxes that cross the air gap have been calculated in Subsection IV-B1 and the total flux is computed

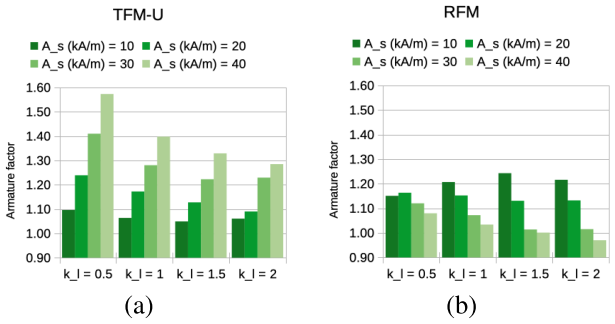

FIGURE 23. FEM armature factor: (a) TFM-U, (b) RFM.

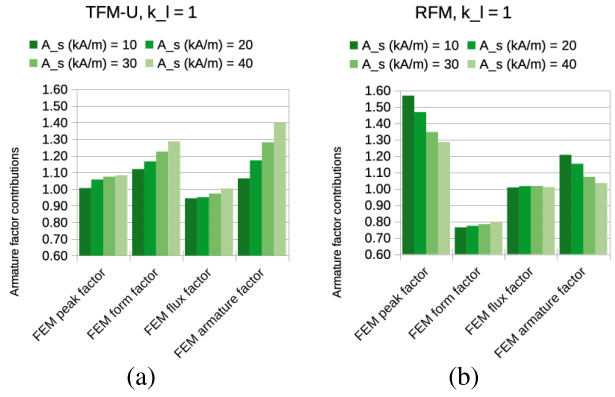

FIGURE 24. Contributions to the FEM armature factor: (a) TFM-U with $k_l = 1$, (b) RFM with $k_l = 1$.

by FEM software. Figure 25 illustrates the comparison between analytical and FEM leakage factors, showing a better agreement in case of the RFM. The calculation of the leakage permeances is based on a simplified geometrical description, thus introducing some error, and the end-winding leakage permeance has a great uncertainty, so the proposed analytical model results can be considered as acceptable. Furthermore, in case of TFMs stator bridges performance (that is, the biggest contribution to leakage according to Table 8) a flux distribution other than constant could be considered according to FEM (Figure 26a), as the leakage flux tends to close mostly through the inner boundary producing a non-uniform flux density in the cross-section. In RFMs a flux distribution depending on the radius is considered when calculating the slot permeance, and this flux distribution is in accordance with FEM results of Figure 26b.

3) SATURATION FACTOR

Even though the electrical machines in this work have been designed for unsaturated condition regarding the magnetizing fluxes, leakage flux increases the total flux at the risk of saturating the magnetic circuit. All the previous simulations have been repeated using a nonlinear material (Cogent M250-35A electrical steel), having similar results for linear and nonlinear simulations. The only exception is the armature

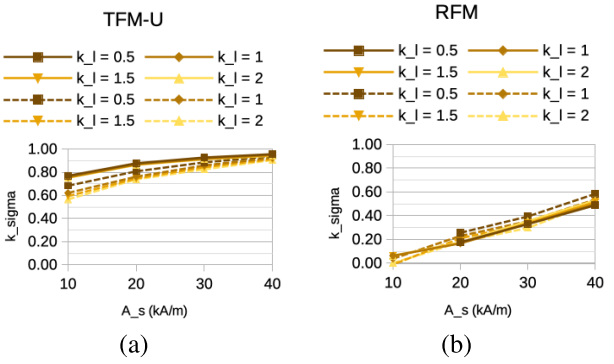

FIGURE 25. Leakage factor, analytical (solid lines) and FEM (dashed line): (a) TFM-U, (b) RFM.

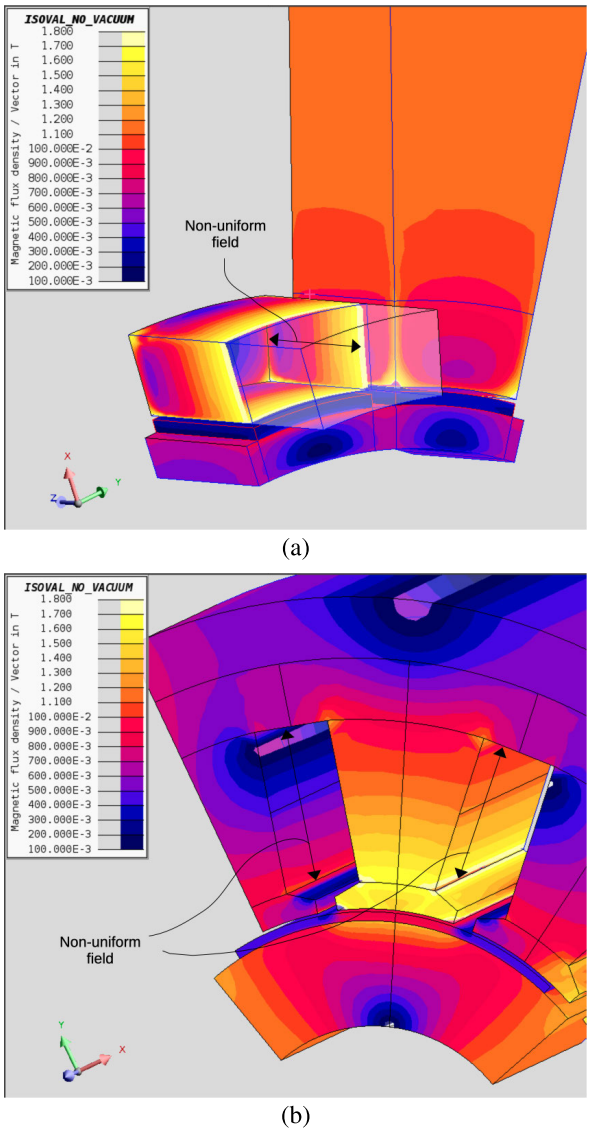

FIGURE 26. FEM flux density: (a) TFM-U with $A_s = 20\,\text{kA/m}$, $k_l = 1$, (b) RFM with $A_s = 20\,\text{kA/m}$, $k_l = 1$.

flux, so a saturation factor k_{sat} (Figure 27) has been calculated —dividing the nonlinear results by the linear results— to correct the sizing equations later.

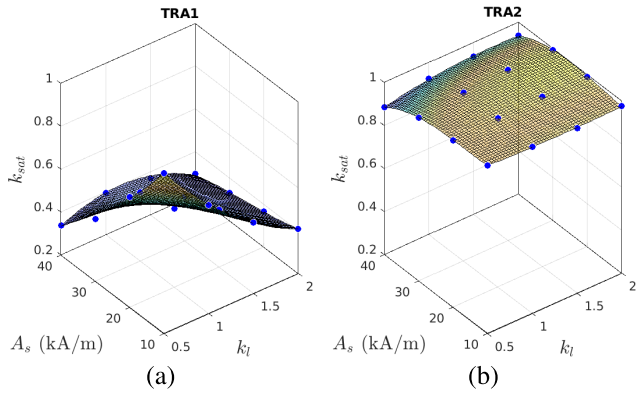

FIGURE 27. FEM saturation factor, surface fitting: (a) TFM-U, (b) RFM.

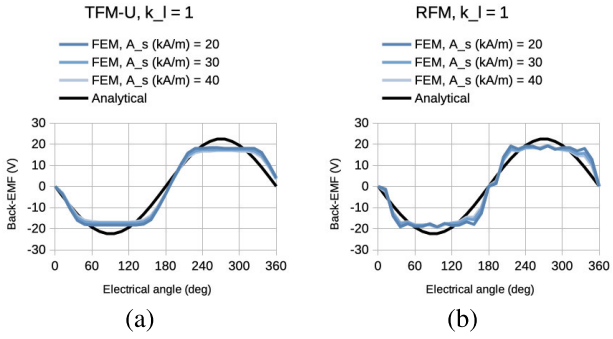

FIGURE 28. Back-EMF: (a) TFM-U with $k_l = 1$, (b) RFM with $k_l = 1$.

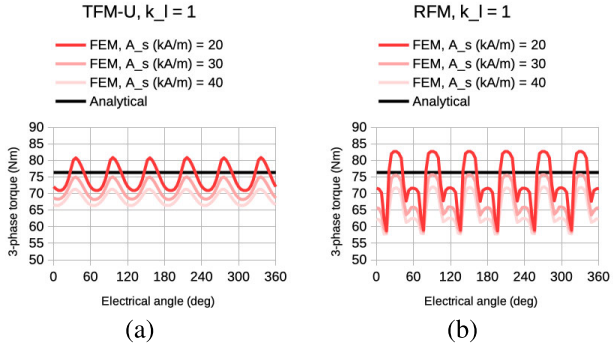

FIGURE 29. Three-phase torque: (a) TFM-U with $k_l = 1$, (b) RFM with $k_l = 1$.

C. BACK-EMF AND BASE TORQUE, DYNAMIC SIMULATIONS

As the machine torque follows (6), the analytical and FEM discrepancies in the first harmonic of the back-EMF and synchronous torque are given by the no-load flux factor. According to Figure 28 and Figure 17, the back-EMF and torque obtained via FEM agree with the analytical first-harmonic analysis, so it has been proved to be accurate enough to size TFMs and RFMs as a first approach. The rest of effects related to harmonics (such as the cogging torque) should be optimized via FEM at a later stage in the design process.

TABLE 10. Design variables ranges.

Design variables (x)	Lower bounds (l)	Upper bounds (u)
k_l	0.5	2
A_s	10 kA/m	40 kA/m
k_{gma}	2	10
k_{wss} (TFM)	0.5	5

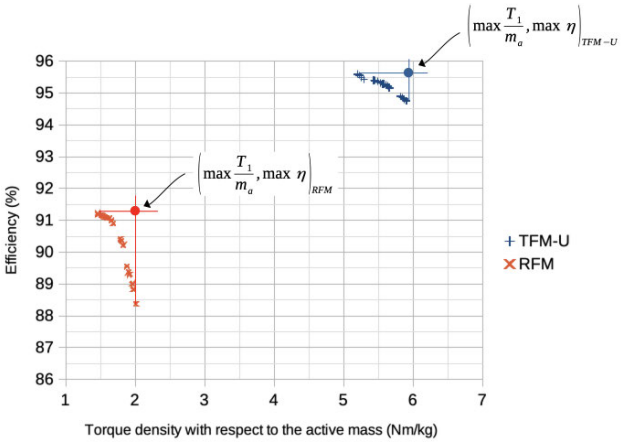

FIGURE 30. Pareto fronts of the multiobjective genetic algorithm optimization.

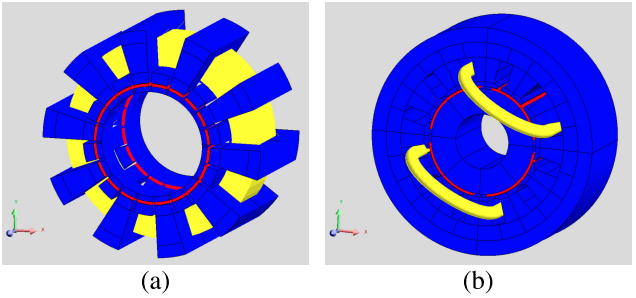

FIGURE 31. Optimum designs from the Pareto front: (a) TFM-U (single-phase model), (b) RFM.

V. OPTIMIZATION

Once the no-load, armature, leakage and saturation factors have been obtained via FEM, their surface equations (88) are introduced in the analytical model and then it is optimized. The optimization problem is presented in (89), the objective functions are the torque density with respect to the active mass T/m_a and the efficiency η (90). The constraints are related to minimum dimensions for manufacturing, performance and the aspect ratio (91), but any other constraints could be included depending on the specific application, such as the overall cost or PMs volume. The design variables are (92), their ranges shown in Table 10. A MATLAB-based multiobjective genetic algorithm (which is a controlled elitist genetic algorithm, a variant of NSGA-II) has been used to solve the problem. The population size, the number of generations, and the mutation function have been left by

TABLE 11. Optimum designs.

	TFM-U	RFM
k_l	1.61	0.73
A_s (kA/m)	20013	17832
k_{gma}	6.4	6.3
k_{wss}	2.7	-
T_1/m_a (Nm/kg)	5.9	1.98
η (%)	94.7	88.8
D_g (cm)	8.4	13.0
l (cm)	2.1	9.5
g_a (mm)	0.3	0.4
g_m (mm)	2.1	2.8
w_{st} (mm)	11	18
w_{ss} (mm)	36	16
h_{ss} (mm)	20	29
D_o (cm)	15.8	26.9
l_o (cm)	23.7	9.5
V_0 (l)	4.6	5.4
m_a (kg)	12.9	38.6
k_0, from (88)	0.9475	1.0049
k_0, from FEM	1.0525	1.0596
k_{ad}, from (88)	1.1155	1.1717
k_{ad}, from FEM	1.0838	0.9710
k_σ, from (88)	0.7406	0.2135
k_σ, from FEM	0.6904	0.0988

default.

$$\begin{aligned} &\underset{\boldsymbol{x}}{\text{maximize}} && f_i(\boldsymbol{x}),\ i = 1, \ldots, m \\ &\text{subject to} && g_j(\boldsymbol{x}) \leq 0,\ j = 1, \ldots, n \end{aligned}$$

$$\boldsymbol{l} \leq \boldsymbol{x} \leq \boldsymbol{u} \tag{89}$$

$$f_1(\boldsymbol{x}) = T_1/m_a \quad \text{and} \quad f_2(\boldsymbol{x}) = \eta \tag{90}$$

$$\begin{aligned} g_1(\boldsymbol{x}) &= 10 - w_{st}(\boldsymbol{x}) \Rightarrow w_{st}(\boldsymbol{x}) \geq 10\,\text{mm} \\ g_2(\boldsymbol{x}) &= 10 - w_{ss}(\boldsymbol{x}) \Rightarrow w_{ss}(\boldsymbol{x}) \geq 10\,\text{mm} \\ g_3(\boldsymbol{x}) &= 0.3 - g_a(\boldsymbol{x}) \Rightarrow g_a(\boldsymbol{x}) \geq 0.3\,\text{mm} \\ g_4(\boldsymbol{x}) &= 1.0 - g_m(\boldsymbol{x}) \Rightarrow g_m(\boldsymbol{x}) \geq 1.0\,\text{mm} \\ g_5(\boldsymbol{x}) &= 80 - \eta(\boldsymbol{x}) \Rightarrow \eta(\boldsymbol{x}) \geq 80\,\% \\ g_6(\boldsymbol{x}) &= k_{loDo}(\boldsymbol{x}) - 1.5 \Rightarrow k_{loDo}(\boldsymbol{x}) \geq 1.5 \end{aligned} \tag{91}$$

$$\boldsymbol{x} = \begin{cases} [k_l, A_s, k_{gma}, k_{wss}] & \text{for TFMs} \\ [k_l, A_s, k_{gma}] & \text{for RFMs} \end{cases} \tag{92}$$

Figure 30 illustrates the Pareto front as a result of solving (89) both for the TFM and the RFM. It is clearly shown that for the proposed optimization problem the TFM is the most favorable option both in terms of torque density and efficiency. From the Pareto sets of optimal solutions, the optimal solution has been chosen for each machine topolgy as the one that minimizes the distance to the —theoretical— point in with both the torque density and the efficiency are maximum, according to (93). The optimum designs taken from the Pareto fronts are shown in Figure 31, and Table 11 collects their main parameters. It is shown that both the torque density and the efficiency have been improved with respect to the machines given by the parametric study. The introduction a priori of the no-load, armature, saturation and leakage factors from surface fitting has allowed to consider these effects in the analytical model, and now the results given by FEM seem to be more optimistic than the analytical predictions in terms of the leakage flux. inally, Table 12 compares optimum designs of this work with other PMSMs in the literature, showing good agreement. The range of active torque densities from previous publications is quite wide, and it depends strongly on specific topologies. As an example, the use of inner permanent magnets in RFMs increases active torque density up to about 10 Nm/kg [40], it is four times higher than the surface-mounted PMSM in [41].

TABLE 12. Optimum designs and other PMSMs in the literature.

	Ref.	Active torque density (Nm/kg)	Efficiency (%)
TFM	Henneberger *et al.*, 1997 - [42]	16	$\simeq 93$
	Wan *et al.*, 2015 - [43]	3.5	85
	Pourmoosa *et al.*, 2018 - [13]	0.86 (1)	86
	This work	5.9	94.7
RFM	Martínez, 2012 - [41]	2.42 (2)	82.2
	Gundogdu *et al.*, 2022 - [40]	9.79 (3)	85.5
	Lerch *et al.*, 2023 - [32]	0.9	-
	This work	1.98	88.8

Note:
Some of the torque densities have been calculated from data in references.
(1) Active power density 135.5 W/kg, speed 1500 rpm
(2) Torque 7 Nm, active mass 2.89 kg
(3) Torque 222.38 Nm, active mass 22.7 kg

$$\min \sqrt{\left(1 - \frac{T_1/m_a}{\max\,(T_1/m_a)}\right)^2 + \left(1 - \frac{\eta}{\max\,(\eta)}\right)^2} \tag{93}$$

VI. CONCLUSION

Transverse flux machines (TFMs) benefit from higher torque density when a high number of pole pairs is used. This is due to their single-phase, hoop-shaped coils that embrace simultaneously the flux of all the pole pairs, unlike radial flux machines (RFMs) where each coil embraces the flux of a single pole pair. Therefore, sizing equations for TFMs differ from those proposed for radial flux machines in the literature. In this work is has been shown that the main dimensions of TFMs can be written as functions of the current load, as in classical theory for radial flux machines. Moreover, the similarity equations introduced here allow a straightforward comparison of TFMs and RFMs, given the specifications and design parameters.

The finite element method (FEM) has been used to quantify the discrepancies between computational models and the analytical assumptions, defining several FEM factors. The analytical model and FEM show a good agreement, thereby a surface-fitting model has been applied to introduce the FEM factors in a second stage of the design process. Finally the analytical model has been optimized using a multiobjective genetic algorithm, proving that TFMs have a superior performance than radial flux machines in terms of torque density and efficiency.

ACKNOWLEDGMENT

This work has been done during a research stay at Mondragon Unibertsitatea. The authors from the University of Zaragoza would like to express their gratitude to the Research Group in Drive Systems Applied to Traction and the Generation of Electric Energy, from Mondragon Unibertsitatea, for their kind reception and support. The authors from University of Zaragoza would also like to show their gratitude to the Government of Aragon for the support received as a recognized research group in the Autonomous Community.

REFERENCES

[1] V. Ballestín-Bernad, J. S. Artal-Sevil, and J. A. Domínguez-Navarro, "A review of transverse flux machines topologies and design," *Energies*, vol. 14, no. 21, p. 7173, Nov. 2021.

[2] S. Huang, J. Luo, and T. A. Lipo, "Analysis and evaluation of the transverse flux circumferential current machine," in *Proc. IAS 97. Conf. Rec. IEEE Ind. Appl. Conf. 32nd IAS Annu. Meeting*, 1997, pp. 378–384.

[3] T. Husain, I. Hasan, Y. Sozer, I. Husain, and E. Muljadi, "Cogging torque minimization in transverse flux machines," *IEEE Trans. Ind. Appl.*, vol. 55, no. 1, pp. 385–397, Jan. 2019.

[4] J. R. Anglada and S. M. Sharkh, "Analysis of transverse flux machines using a virtual mutual inductance approach," *IEEE Trans. Energy Convers.*, vol. 33, no. 2, pp. 465–472, Jun. 2018.

[5] M. Schmid, J. Terfurth, K. Kaiser, and N. Parspour, "Electromagnetic design of electrical machines—New potentials of additive manufacturing with the example of the transverse flux machine," in *Proc. Int. Conf. Electr. Mach. (ICEM)*, Sep. 2022, pp. 1491–1497.

[6] V. Ballestín-Bernad, J. S. Artal-Sevil, and J. A. Domínguez-Navarro, "Prototype of a two-phase axial-gap transverse flux generator based on reused components and 3D printing," *Energies*, vol. 16, no. 4, p. 1594, Feb. 2023.

[7] T. Husain, I. Hasan, Y. Sozer, I. Husain, and E. Muljadi, "Design considerations of a transverse flux machine for direct-drive wind turbine applications," *IEEE Trans. Ind. Appl.*, vol. 54, no. 4, pp. 3604–3615, Jul. 2018.

[8] A. Chowdhury and Y. Sozer, "Design and analysis of a hook shaped stator core with ring winding transverse flux machine for wind turbine applications," in *Proc. IEEE Energy Convers. Congr. Expo. (ECCE)*, Oct. 2020, pp. 540–544.

[9] A. Chowdhury, S. Das, T. Tsuda, N. Saito, S. Saha, and Y. Sozer, "Design and analysis of a high saliency transverse flux machine with a novel rotor structure for traction applications," in *Proc. IEEE Energy Convers. Congr. Expo. (ECCE)*, Oct. 2020, pp. 1743–1748.

[10] J. R. Anglada and S. M. Sharkh, "An insight into torque production and power factor in transverse-flux machines," *IEEE Trans. Ind. Appl.*, vol. 53, no. 3, pp. 1971–1977, May 2017.

[11] J. Renedo Anglada and S. M. Sharkh, "Analytical calculation of the torque produced by transverse flux machines," *IET Electr. Power Appl.*, vol. 11, no. 7, pp. 1298–1305, Aug. 2017.

[12] M. A. Hernández-Rodríguez, R. Iracheta-Cortez, N. Flores-Guzmán, E. Hernández-Mayoral, R. Gómez-Torres, and W. Durante-Gómez, "Designing a transverse flux PMSG with analytical methods for applications in wind turbines," in *Proc. IEEE 38th Central Amer. Panama Conv. (CONCAPAN)*, Nov. 2018, pp. 1–9.

[13] A. A. Pourmoosa and M. Mirsalim, "A transverse flux generator with a single row of permanent magnets: Analytical design and performance evaluation," *IEEE Trans. Ind. Electron.*, vol. 66, no. 1, pp. 152–161, Jan. 2019.

[14] A. A. Pourmoosa, M. Mirsalim, A. Mahmoudi, and S. Vaez-Zadeh, "Analytical model based on magnetic equivalent circuit for transverse-flux permanent-magnet machines," *Int. Trans. Electr. Energy Syst.*, vol. 30, Jul. 2020, Art. no. e12414.

[15] R. Nasiri-Zarandi, A. M. Ajamloo, and K. Abbaszadeh, "Proposing the output equations and 3-D MEC modeling for U-core TFPM generators," in *Proc. Int. Symp. Power Electron., Electr. Drives, Autom. Motion (SPEEDAM)*, Jun. 2018, pp. 292–297.

[16] A. M. Ajamloo, A. Ghaheri, and R. Nasiri-Zarandi, "Design and optimization of a new TFPM generator with improved torque profile," in *Proc. Int. Power Syst. Conf. (PSC)*, Dec. 2019, pp. 106–112.

[17] G. Peng, J. Wei, Y. Shi, Z. Shao, and L. Jian, "A novel transverse flux permanent magnet disk wind power generator with H-shaped stator cores," *Energies*, vol. 11, no. 4, p. 810, Mar. 2018.

[18] C. Lv, L. Zhang, Y. Xu, and Y. Liu, "Research on novel high torque density transverse-flux permanent magnet motor," in *Proc. 22nd Int. Conf. Electr. Mach. Syst. (ICEMS)*, Aug. 2019, pp. 1–5.

[19] M. Kremers, "Analytical design of a transverse flux machine," Ph.D. thesis, Eindhoven Univ. Technol., Eindhoven, The Netherlands, 2016.

[20] Z. Wan and I. Husain, "Design, analysis and prototyping of a flux switching transverse flux machine with ferrite magnets," in *Proc. IEEE Energy Convers. Congr. Expo. (ECCE)*, Oct. 2017, pp. 1227–1233.

[21] B. Boomiraja and R. Kanagaraj, "A novel hybrid flux machine with transverse flux stator and longitudinal flux rotor: Design and comparative analysis," *Electr. Eng.*, vol. 102, no. 3, pp. 1413–1422, Sep. 2020.

[22] V. Ballestín-Bernad, J. S. Artal-Sevil, and J. A. Domínguez-Navarro, "Analytical optimal design of a two-phase axial-gap transverse flux motor," *Energies*, vol. 14, no. 12, p. 3666, Jun. 2021.

[23] *SMC Cores in Honda's Prototype Transverse Flux Motor for Hybrid Powertrains*. Accessed: Oct. 16, 2021. [Online]. Available: https://www.PM-review.com/smc-cores-in-hondas-prototype-transverse-flux-motor-for-hybrid-powertrains/

[24] A. M. A. Elantably, "An approach to sizing high power density TFPM intended for hybrid bus electric propulsion," *Electr. Mach. Power Syst.*, vol. 28, no. 4, pp. 341–354, Apr. 2000.

[25] A. J. Mitcham, "Transverse flux motors for electric propulsion of ships," in *Proc. IEE Colloq. New Topologies Permanent Magnet Mach.*, 1997, pp. 1–6.

[26] *GKN Powder Metallurgy: Transverse Flux Motors (TFM) Solution*. Accessed: Jul. 16, 2023. [Online]. Available: https://youtu.be/1XqRV4no6TA

[27] *NOVUS Electric Motorcycle Lightness and Power*. Accessed: Jul. 16, 2023. [Online]. Available: https://novusbike.com/bike-2/

[28] S. T. Lundmark and P. R. Fard, "Two-dimensional and three-dimensional core and magnet loss modeling in a radial flux and a transverse flux PM traction motor," *IEEE Trans. Ind. Appl.*, vol. 53, no. 3, pp. 2028–2039, May 2017.

[29] I. Martinez-Ocaña, N. J. Baker, B. C. Mecrow, C. Hilton, and S. Brockway, "Transverse flux machines as an alternative to radial flux machines in an in-wheel motor," *J. Eng.*, vol. 2019, no. 17, pp. 3624–3628, Jun. 2019.

[30] B. Zhang, T. Epskamp, M. Doppelbauer, and M. Gregor, "A comparison of the transverse, axial and radial flux PM synchronous motors for electric vehicle," in *Proc. IEEE Int. Electr. Vehicle Conf. (IEVC)*, Dec. 2014, pp. 1–6.

[31] T. Drabek, P. Kapustka, T. Lerch, and J. Skwarczyński, "A novel approach to transverse flux machine construction," *Energies*, vol. 14, no. 22, p. 7690, Nov. 2021.

[32] T. Lerch, "Analysis of the impact of design parameters on the power density of the new design of the cogging machine," *Energies*, vol. 16, no. 7, p. 3000, Mar. 2023.

[33] P. Krause, O. Wasynczuk, S. Sudhoff, and S. Pekarek, *Analysis of Electric Machinery and Drive Systems*, 3 ed. Piscataway, NJ, USA: IEEE, 2013.

[34] M. C. Kulan, N. J. Baker, and S. Turvey, "Manufacturing challenges of a modular transverse flux alternator for aerospace," *Energies*, vol. 13, no. 16, p. 4275, Aug. 2020.

[35] M. C. Kulan, N. J. Baker, and S. Turvey, "Impact of manufacturing and material uncertainties in performance of a transverse flux machine for aerospace," *Energies*, vol. 15, no. 20, p. 7607, Oct. 2022.

[36] V. Ballestín-Bernad, J. S. Artal-Sevil, and J. A. Domínguez-Navarro, "Analytical design methodology for wind power permanent magnet synchronous generators," *Renew. Energy Power Qual. J.*, vol. 21, no. 1, pp. 606–612, Jul. 2023.

[37] J. Corrales-Martín, *Cálculo Industrial de Máquinas Eléctricas*, vol. 1. Barcelona, Spain: Marcombo, 1982.

[38] J. Pyrhonen, T. Jokinen, and V. Hrabovcova, *Design of Rotating Electrical Machines*, 1st ed. Hoboken, NJ, USA: Wiley, 2008.

[39] J. F. Gieras, *Permanent Magnet Motor Technology Design and Applications*, 3 ed. Boca Raton, FL, USA: CRC Press, 2010.

[40] T. Gundogdu, Z.-Q. Zhu, and C. C. Chan, "Comparative study of permanent magnet, conventional, and advanced induction machines for traction applications," *World Electr. Vehicle J.*, vol. 13, no. 8, p. 137, Jul. 2022.

[41] D. Martínez, "Design of a permanent-magnet synchronous machine with non-overlapping concentrated windings for the shell eco marathon urban prototype," M.S. thesis, KTH Roy. Inst. Technol., Stockholm, Sweden, 2012.
[42] G. Henneberger, "Development of a new transverse flux motor," in *Proc. IEE Colloq. New Topologies Permanent Magnet Mach.*, 1997, pp. 1–6.
[43] Z. Wan, A. Ahmed, I. Husain, and E. Muljadi, "A novel transverse flux machine for vehicle traction aplications," in *Proc. IEEE Power Energy Soc. Gen. Meeting*, Jul. 2015, pp. 1–5.

VÍCTOR BALLESTÍN-BERNAD was born in Zaragoza, Spain, in 1996. He received the B.Sc. degree in industrial technologies engineering, the M.Sc. degree in industrial engineering, and the M.Sc. degree in teaching from the University of Zaragoza, Spain, in 2018, 2020, and 2021, respectively, where he is currently pursuing the Ph.D. degree in renewable energies and energy efficiency.

From 2017 to 2018, he was with the Department of Electrical Engineering, University of Zaragoza, under a collaboration fellowship granted by the Spanish Ministry of Education. His current research interests include the design and simulation of electric machines, especially transverse flux machines, and vehicle traction systems.

ARITZ EGEA-CÁCERES received the master's and Ph.D. degrees in electrical engineering from the University of Mondragon, Mondragon, Spain, in 2009 and 2012, respectively.

He is currently an Associate Professor with the Faculty of Engineering, Mondragon Unibertsitatea. His current research interests include electrical machine design and control and electromagnetic actuators.

JESÚS SERGIO ARTAL-SEVIL received the B.Sc. degree in industrial engineering (electrical), the M.Sc. degree in renewable energies and energy efficiency, and the M.Sc. degree in electronic engineering from the University of Zaragoza, Spain, in 1997, 2014, and 2016, respectively.

He was a Design and Development Engineer with the Electronic Technology and Electric Vehicle Division, from 1997 to 2001, in the automotive industry. He is currently a Researcher and full-time Professor with the Department of Electrical Engineering, School of Engineering and Architecture, University of Zaragoza. Since then, he has participated in different research projects in the fields of renewable energy applications, hybrid energy storage systems (hESS), and off-grid systems. Currently, he is the author or co-author of more than 100 scientific articles in journals and conference papers. His current research interests include power electronics, resonant and soft-switched power converters, modeling and control of converters, design and simulation of electrical machines for vehicle traction, solid-state transformers, FACTS, and power conversion applications.

JOSÉ ANTONIO DOMÍNGUEZ-NAVARRO (Senior Member, IEEE) was born in Zaragoza, Spain, in 1966. He received the Ph.D. degree in electrical engineering from the University of Zaragoza, Spain, in 2000.

In 1992, he joined the University of Zaragoza, where he is currently a Full Professor with the Electrical Engineering Department. He has been involved in some research projects related to the optimization of power distribution networks, the modeling of electrical machines, and artificial intelligence applications in electrical engineering. His current research interests include the applications of soft computing in electric power systems, power distribution network planning, electric machines, and metaheuristic optimization.